NASA/TM—2016-219419

Full-Scale Turbofan Engine Noise-Source Separation Using a Four-Signal Method

Lennart S. Hultgren
Glenn Research Center, Cleveland, Ohio

Rene O. Arechiga
New Mexico Tech, Socorro, New Mexico

November 2016

NASA STI Program . . . in Profile

Since its founding, NASA has been dedicated to the advancement of aeronautics and space science. The NASA Scientific and Technical Information (STI) Program plays a key part in helping NASA maintain this important role.

The NASA STI Program operates under the auspices of the Agency Chief Information Officer. It collects, organizes, provides for archiving, and disseminates NASA's STI. The NASA STI Program provides access to the NASA Technical Report Server—Registered (NTRS Reg) and NASA Technical Report Server—Public (NTRS) thus providing one of the largest collections of aeronautical and space science STI in the world. Results are published in both non-NASA channels and by NASA in the NASA STI Report Series, which includes the following report types:

- TECHNICAL PUBLICATION. Reports of completed research or a major significant phase of research that present the results of NASA programs and include extensive data or theoretical analysis. Includes compilations of significant scientific and technical data and information deemed to be of continuing reference value. NASA counter-part of peer-reviewed formal professional papers, but has less stringent limitations on manuscript length and extent of graphic presentations.

- TECHNICAL MEMORANDUM. Scientific and technical findings that are preliminary or of specialized interest, e.g., "quick-release" reports, working papers, and bibliographies that contain minimal annotation. Does not contain extensive analysis.

- CONTRACTOR REPORT. Scientific and technical findings by NASA-sponsored contractors and grantees.

- CONFERENCE PUBLICATION. Collected papers from scientific and technical conferences, symposia, seminars, or other meetings sponsored or co-sponsored by NASA.

- SPECIAL PUBLICATION. Scientific, technical, or historical information from NASA programs, projects, and missions, often concerned with subjects having substantial public interest.

- TECHNICAL TRANSLATION. English-language translations of foreign scientific and technical material pertinent to NASA's mission.

For more information about the NASA STI program, see the following:

- Access the NASA STI program home page at http://www.sti.nasa.gov

- E-mail your question to help@sti.nasa.gov

- Fax your question to the NASA STI Information Desk at 757-864-6500

- Telephone the NASA STI Information Desk at 757-864-9658

- Write to:
  NASA STI Program
  Mail Stop 148
  NASA Langley Research Center
  Hampton, VA 23681-2199

NASA/TM—2016-219419

Full-Scale Turbofan Engine Noise-Source Separation Using a Four-Signal Method

Lennart S. Hultgren
Glenn Research Center, Cleveland, Ohio

Rene O. Arechiga
New Mexico Tech, Socorro, New Mexico

National Aeronautics and
Space Administration

Glenn Research Center
Cleveland, Ohio 44135

November 2016

Acknowledgments

This work is supported by the NASA Advanced Air Vehicles Program, Advanced Air Transport Technology Project, Aircraft Noise Reduction Subproject and the 2016 NASA Glenn Faculty Fellowship Program.

Level of Review: This material has been technically reviewed by technical management.

Available from

NASA STI Program
Mail Stop 148
NASA Langley Research Center
Hampton, VA 23681-2199

National Technical Information Service
5285 Port Royal Road
Springfield, VA 22161
703-605-6000

This report is available in electronic form at http://www.sti.nasa.gov/ and http://ntrs.nasa.gov/

Full-Scale Turbofan Engine Noise-Source Separation Using a Four-Signal Method

Lennart S. Hultgren
National Aeronautics and Space Administration
Glenn Research Center
Cleveland, Ohio 44135

Rene O. Arechiga
New Mexico Tech
Socorro, New Mexico 87801

Abstract

Contributions from the combustor to the overall propulsion noise of civilian transport aircraft are starting to become important due to turbofan design trends and expected advances in mitigation of other noise sources. During on-ground, static-engine acoustic tests, combustor noise is generally sub-dominant to other engine noise sources because of the absence of in-flight effects. Consequently, noise-source separation techniques are needed to extract combustor-noise information from the total noise signature in order to further progress. A novel four-signal source-separation method is applied to data from a static, full-scale engine test and compared to previous methods. The new method is, in a sense, a combination of two- and three-signal techniques and represents an attempt to alleviate some of the weaknesses of each of those approaches. This work is supported by the NASA Advanced Air Vehicles Program, Advanced Air Transport Technology Project, Aircraft Noise Reduction Subproject and the NASA Glenn Faculty Fellowship Program.

1 Introduction

Turbofan combustor noise is a low-frequency broadband contributor to the noise generated in the engine core. The turbine and the compressor are two other core-noise sources. In addition, there is noise generated by the fan and the jet. Fig. 1 depicts the evolution of the relative strengths of these noise sources over time. For current generation aircraft engines, core noise can make a significant contribution to the aft-quadrant overall noise signature at low-power conditions, typical of approach. Turbofan core-noise reduction will be needed in the near future because engine-cycle changes and technology advances are expected to further reduce non-core noise components (i.e., fan and jet) at all engine power settings. Proposed low-pressure-turbine designs are expected to increase turbine-noise source strength and complexity as well as reduce the turbine acoustic transmission losses for the combustor noise. Future low-emission combustor designs could also increase the combustor-noise component as well. Taken together, these emerging cycle and design changes will make core noise a significant component of the total engine noise signature, which will need to be addressed in order to meet future aircraft noise-reduction goals. In fact, core noise may well set a noise floor limiting the effects of future mitigation techniques for other propulsion-noise sources if not further controlled.

Groeneweg et al. [1] and Mahan and Karchmer,[2] in the collection by Hubbard,[3] summarize the status and understanding of turbomachinery contributions to flight vehicle noise at the beginning of the 1990's. Whereas jet and fan noise research and understanding have progressed; the state of the art in practical core-noise prediction has not been equally advanced. Low-frequency broadband core noise up to about 1 kHz, particularly in aft quadrants, is generally attributed to combustor noise. Turbine broadband and discrete-tone noise normally falls in the frequency range of

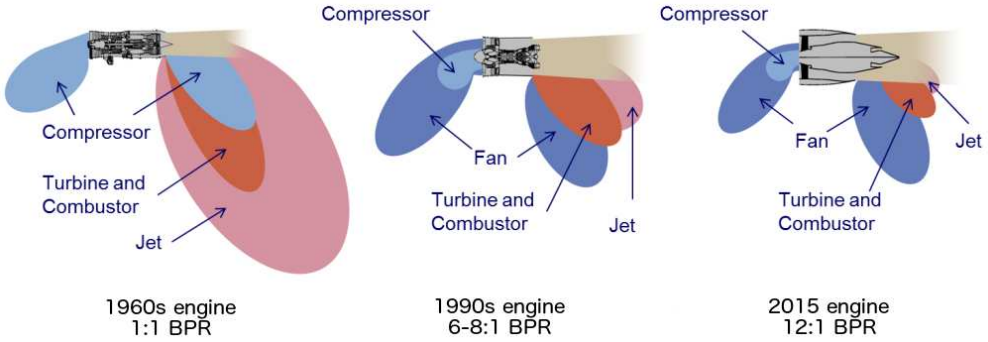

Figure 1. Evolution of propulsion-noise sources over time; original figure courtesy of Pratt & Whitney

several kHz and above. The discrete tones are caused by rotor wakes interacting with downstream stators and, to a lesser extent, potential fields interacting with upstream and downstream blade rows. Internal turbine broadband noise is caused by rotor/stator lift fluctuations due to flow turbulence. However, there is also a significant broadband component in the far field associated with scattering of the discrete turbine tones by turbulence in the jet shear layer(s). This so called hay-stacking effect usually dominates the broadband noise generated within the turbine. Compressor noise occurs mainly in the forward direction as discrete tones at the first stage blade-passing frequency (kHz) or as a compressor-disk tone at the compressor shaft frequency (several hundred Hz). The compressor is commonly not considered a significant noise source for today's high-bypass turbofan engines. The present paper is concerned with the combustor-noise component of the core noise. Summaries of the current status of combustor-noise source modeling, as well as historical perspectives, are given in the review chapters by Mahan and Karchmer,[2] Hultgren et al.[4] (see also Hultgren[5]), Dowling and Mahmoudi,[6] and Ihme.[7]

2 Combustor Noise

The term 'combustor' noise is used here, rather than the more traditional term 'combustion' noise, for two reasons. First, it is used to clearly indicate that this aircraft propulsion-noise component is generated inside the turbofan engine core. Even though it may have many aspects in common with open-flame combustion noise, it is generated in a confined geometry at a higher pressure and it is modified by resonances and transmission effects. Second, combustor noise consists of both direct and indirect components, see Fig. 2. A fraction of the unsteady pressure disturbances

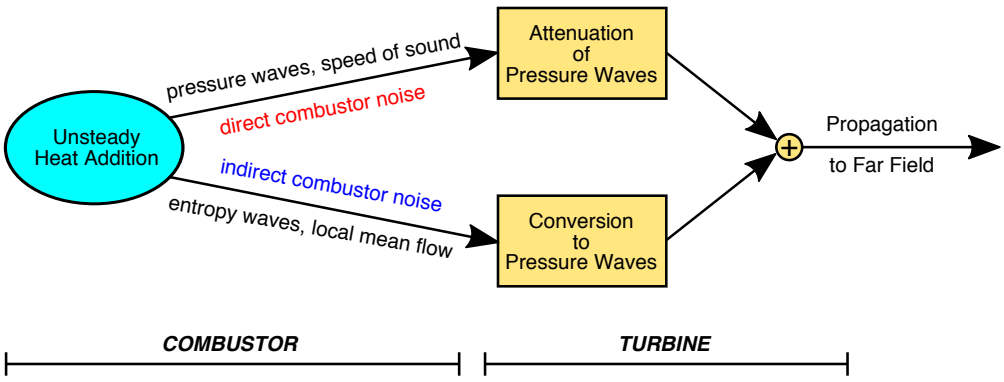

Figure 2. Dual paths for combustor noise

in the combustor are acoustic perturbations caused by the unsteady heat release. This is the direct component of the combustor noise and, as just pointed out, is somewhat related to 'traditional' combustion noise. The balance of the

pressure fluctuations in the combustor are associated with hydrodynamic unsteadiness. The direct combustor noise is reduced due to transmission effects as it propagates through the turbine and engine ducts. The unsteady combustion process also produces entropy and vorticity fluctuations. These perturbations are both convected downstream with the local mean velocity and can produce acoustic perturbations in the turbine and other regions where flow properties change rapidly. The conversion of entropy fluctuations to noise is generally believed to be the stronger effect and is referred to as the indirect-noise mechanism. The indirect noise occurs in the same basic frequency range as the direct one, since they are both driven by the unsteady heat release of the combustion process. However, their spectral-distribution shapes could be quite different. The peak frequency on an 1/3-octave basis for the direct combustor noise commonly falls in the range of 400–500 Hz, whereas no such consensus has been reached for the indirect combustor noise. The relative importance of direct and indirect combustion noise is still also an unresolved issue. Nevertheless, it is clear that the combustor and turbine ultimately need to be treated as a (loosely, at minimum) coupled system in order to improve the physical understanding of the source structure of combustor noise, which is essential for the advancement of airport community-noise prediction capability as well as strategies for combustor-noise mitigation.

The direct measurement of turbofan-engine combustor noise is difficult because of the presence of jet noise in the frequency range of interest. Since in-flight effects reduce jet noise more than combustor noise, combustor noise can be a significant contributor to aircraft-approach noise but masked by jet noise under the corresponding static-engine test condition. To overcome this obstacle, researchers[8–17] developed coherence techniques utilizing engine-internal as well as far-field measurements to identify the far-field combustion noise component. Modal analyses[18–21] were also carried out to determine the source and propagation characteristics of combustor noise. In this report, a new four-signal source-separation technique is applied to existing engine test-stand acoustic data[22] and compared with previous results.[23–25] The method combines two- and three-signal approaches in an attempt to alleviate some of their inherent weaknesses.

3 Static-Engine Acoustic Test Data

The test data used herein are from configuration 35 of the NASA/Honeywell Engine Validation of Noise and Emission Reduction Technology program[22] (EVNERT). The EVNERT static engine test activity was carried out in Honeywell Aerospace's San Tan outdoor test facility from 2005 to 2007. The program used the Honeywell TECH977 turbofan research engine, which is typical of a business-jet application in the 6,000–8,000 lbs thrust class. The engine-internal instrumentation in the EVNERT test included high-temperature pressure sensors with air cooling in a combustor ignitor port (CIP1) and at the turbine exit (T551 and T552)—all indicated with red arrows in Fig. 3. Pressure time histories at these sensors and aft-quadrant far-field microphones are used here. The spectral response of the engine-internal-sensor arrangements was deemed sufficiently flat in the combustor-noise frequency range of interest.[22] Consequently, spectral compensation of the raw engine-internal measurements is not needed here. The EVNERT data acquisition system had a sampling rate of 65,536 Hz and a duration of about 70 s, leading to time histories with just over 4.5 million data points. Each time series is analyzed here using an FFT length of 8192 points (corresponding to an 8 Hz frequency resolution or bin width), Hamming windowing, and various data-segment overlaps. The resulting averaged narrow-band auto spectra can be summed up to yield the corresponding 1/3-octave sound-pressure level (SPL). The 130° polar direction, measured from the inlet, far-field total-signal 1/3-octave SPL results were found to be in full agreement with the Honeywell provided 1/3-octave SPL data.[24]

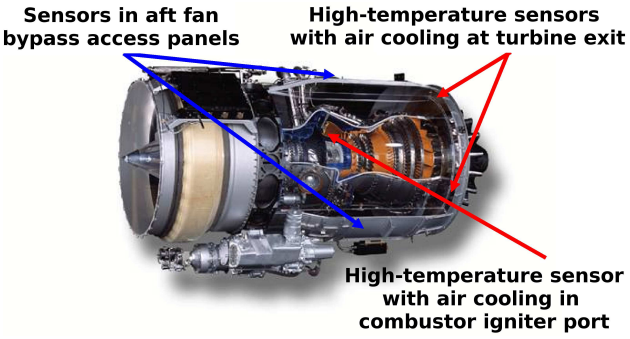

Figure 3. Honeywell TECH977 turbofan engine-internal sensors

Royalty and Schuster[26] analyzed the acoustic modes in the combustor for a different arrangement of the EVNERT turbofan engine than considered herein. In that configuration,[22] the fan was replaced by a water brake in order to remove fan sources from the total noise signature. The no-fan configuration could be operated up to a power

setting corresponding to the approach condition of 60 % corrected fan speed. The combustor internal instrumentation consisted of a circumferential array of 16 equally-spaced pressure probes. They[26] (see their Fig. 19) found that for low frequencies most of the acoustic energy in the combustor was associated with the plane wave ($m = 0$) mode, that the first circumferential mode ($m = \pm 1$) was dominant in the frequency range of 500–1000 Hz, and that higher circumferential modes ($m = \pm 2$, $m = \pm 3$, ...) sequentially became the most significant feature at successively higher frequencies, where m is the azimuthal wave number or mode order. One can observe in their figure that at 500 Hz, the plane wave mode is about 8 dB and 5 dB below the total acoustic level at the 48 % and 60 % power settings, respectively. They also reported that the higher modes ($m \neq 0$) were not present in the far-field data. This indicates that the non-plane-wave modes are cut-off in the turbine/duct downstream of the combustor for this particular engine. This is in agreement with the results of Hultgren and Miles[24] in which coherent combustor noise was only found for frequencies less than about 400+ Hz.

4 Data Analysis

Figure 4 illustrates the relationships between the signals measured by the three engine-internal sensors CIP1, T551, and T552 and the far-field microphones located at the polar angles of 110°, 130°, and 160° that will be used here.

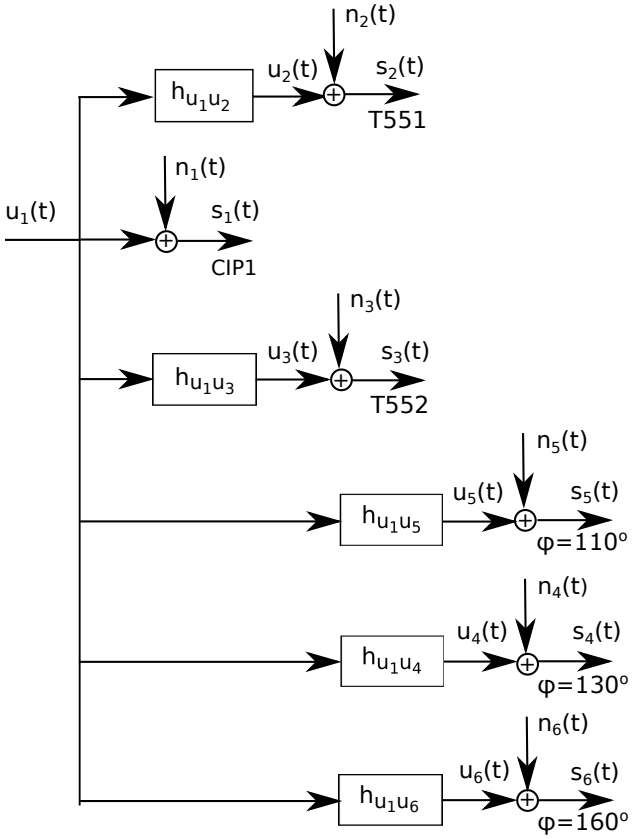

Figure 4. Coherence-technique schematic

The signals $u_i(t)$, $i = 1,2,\ldots,6$, represent the coherent acoustic combustor-noise signal at the sensor locations as functions of time t. Of these, $u_1(t)$ is considered the source signal. The signals $u_i(t)$, $i = 2,3,\ldots,6$, are uniquely determined by the source signal $u_1(t)$ and the corresponding impulse-response function $h_{u_1u_i}$. These 'desired' signals cannot be directly obtained by themselves because of the presence of the random uncorrelated 'noise' signals $n_i(t)$, $i = 1,2,\ldots,6$, at the different measuring stations. The measurable signals, $s_i(t) = u_i(t) + n_i(t)$, $i = 1,2,\ldots,6$, at each sensor are the sum of the 'desired' and corresponding 'noise' signals. The signals $n_i(t)$ are assumed to be mutually uncorrelated as well as uncorrelated with all the combustor-noise signals $u_i(t)$.

The signal $n_1(t)$ is to a large extent caused by hydrodynamic pressure fluctuations (pseudo-sound) in the combustor and possibly also higher acoustic modes present in the combustor but cut-off in the downstream tail pipe and can potentially be quite large. The signals $n_i(t)$, $i = 2,3,\ldots,6$, are mainly due to acoustic pressure fluctuations from other noise sources and can actually be correlated if turbine broadband noise is also present at the frequencies of interest. If the far-field microphones are spaced too close together, then the signals $n_i(t)$, $i = 4,5,6$, can also be correlated due to jet noise.

The goal of the present work is to determine the combustor-noise component, $G_{u_4u_4}(f)$, of the measured total noise signature, $G_{44}(f)$, in the 130° polar direction, where f is the frequency and $G_{\alpha\alpha}$ denotes the one-sided auto-spectrum of the signal α. Similarly, $G_{\alpha\beta}$ denotes the one-sided cross-spectrum between the signals α and β. α and β are dummy indexes. Note that for simplicity of notation, only the signal index 'i' is used as a subscript rather than the more complete 's_i' for the measurable signals.

4.1 *Two-Signal-Coherence Method*

The basic derivation of the two-signal, or coherent-output-power, method is described in the textbook by Bendat and Piersol.[8] If the sensor inside the combustor and the 130° far-field microphone (Fig. 4) are used in this technique, it follows that the coherent combustor-noise spectrum at the far-field location is given by

$$G_{u_4u_4}(f) = \frac{|G_{u_1u_4}(f)|^2}{G_{u_1u_1}(f)} = \frac{|G_{14}(f)|^2}{G_{u_1u_1}(f)} \tag{1}$$

regardless of the input noise $G_{n_1n_1}(f)$ and output noise $G_{n_4n_4}(f)$. It is an exact result, but it suffers from the fact that $G_{u_1u_1}$ is not directly measurable. By replacing the unknown input spectrum $G_{u_1u_1}$ with its positive-biased estimate $G_{11} = G_{u_1u_1} + G_{n_1n_1}$, the following two-signal result is obtained:

$$G^{(2s)}_{u_4u_4}(f) = G^{(2s)}_{1-4}(f) = \frac{|G_{14}(f)|^2}{G_{11}(f)} = \gamma^2_{14}(f)G_{44}(f)\,, \tag{2}$$

where $\gamma_{\alpha\beta} = |G_{\alpha\beta}|/\sqrt{G_{\alpha\alpha}G_{\beta\beta}}$ is the coherence and the alternate notation $G^{(2s)}_{1-4}$ is introduced. The superscript '2s' designates a two-signal result and the 'k-n' notation indicates a configuration with sensors 'n' and 'k' considered to be at the observer and source locations, respectively. This result is still independent of the output noise $G_{n_4n_4}$. But, in view of the certain presence of nonpropagating pressure fluctuations in the combustor, i.e., $G_{n_1n_1} \neq 0$, Eq. (2) is quite likely to underpredict the actual coherent output spectrum. The following bounds hold for the actual coherent output power:

$$G^{(2s)}_{u_4u_4}(f) \leq G_{u_4u_4}(f) \leq G_{44}(f)\,. \tag{3}$$

Equations (1) and (2) are specifically for the 1-4 sensor configuration. For the test data considered herein, there are two more possible two-signal configurations involving the 130° far-field microphone and one engine-internal sensor, namely 2-4 and 3-4, see Fig. 4. The coherent-output-power formulas for these cases are analogous to Eq. (2).

4.2 *Three-Signal-Coherence Method*

Chung[27] developed a three-signal coherence technique for microphone flow-noise rejection, which was independently applied by Krejsa,[15–17] using two engine-internal sensors and a far-field microphone, to eliminate the bias error in the far-field coherent combustor-noise measurements due to engine-internal nonpropagating pressure fluctuations. The strength of the standard three-signal method is that it involves only measured cross-spectra. The measured cross-spectra are affected by extraneous noise only if this noise correlates between measurement locations. This can often be avoided by an appropriate spatial separation of the sensors involved and the three-signal method then provides unbiased estimates of the coherent auto-spectrum. In contrast, measured auto-spectra will always include a positive definite contribution from the extraneous noise at the sensor location.

Applying the three-signal method, using the three internal sensors, CIP1, T551, and T552 (Fig. 4), it follows that the coherent auto-spectrum at the CIP1 sensor is given by[25]

$$G^{(3s)}_{u_1u_1}(f) = G^{(3s)}_{23-1}(f) = \frac{G_{21}(f)G^*_{31}(f)}{G_{23}(f)} = \frac{|G_{12}(f)||G_{13}(f)|}{|G_{23}(f)|} = \frac{\gamma_{12}(f)\gamma_{13}(f)}{\gamma_{23}(f)}G_{11}(f)\,, \tag{4}$$

where the star '*' denotes complex conjugation, the superscript '3s' indicates a three-signal method result, and the 'kl-n' notation implies a three-signal configuration with sensor 'n' at the observer location and sensors 'k' and 'l' at the two auxiliary locations.

Using the two internal sensors T551 and T552 and the 130° far-field microphone in the three-signal method (configuration 23-4), it follows that the correlated engine-internal noise at the far-field location is given by[28]

$$G^{(3s)}_{u_4u_4}(f) = G^{(3s)}_{23-4}(f) = \frac{G_{24}(f)G^*_{34}(f)}{G_{23}(f)} = \frac{|G_{24}(f)||G_{34}(f)|}{|G_{23}(f)|} = \frac{\gamma_{24}(f)\gamma_{34}(f)}{\gamma_{23}(f)}G_{44}(f)\,, \tag{5}$$

which Mendoza et al.[23] identifies as one of the two partial-coherence results obtainable by using a five-microphone technique. Two other three-signal configurations involving the 130° far-field microphone and two engine-internal

sensors are possible here, namely 12-4 and 13-4, see Fig. 4. The corresponding three-signal formulas for the coherent output at the far-field microphone for these configurations are analogous to Eq. (5).

It is also possible to separate core noise from jet noise using three far-field microphones since each would pick up correlated core noise and uncorrelated external noise from the jet.[23,29] As long as the spatial (polar angle) separation of the microphones is large enough, the jet noise at each location can be assumed to be mutually uncorrelated and it follows that

$$G^{(3f)}_{u_4u_4}(f) = G^{(3s)}_{56-4}(f) = \frac{G_{54}(f)G^*_{64}(f)}{G_{56}(f)} = \frac{|G_{45}(f)||G_{46}(f)|}{|G_{56}(f)|} = \frac{\gamma_{45}(f)\gamma_{46}(f)}{\gamma_{56}(f)}G_{44}(f)\,, \tag{6}$$

where the superscript '3f' is introduced to indicate that three far-field microphones are used (56-4 configuration).

It is well known[30–32] that the three-signal method fails to produce reliable results in frequency ranges where more than one coherent source, or signal, are present. Minami and Ahuja[30] were the first to carefully document this weakness by analyzing the situation where two coherent signals are buried in noise. For the special case when the relative strength of the two coherent sources is unchanged for all three measuring locations, their derivation showed that a separation of about 10 dB would be needed in order for the three-signal technique to reliably detect the stronger signal (within 3 dB) and that the error would be very large as the two become of comparable magnitude, see their Fig. 3. Minami and Ahuja[30] also carried out a numerical simulation of a generic/simplified situation involving two coherent signals buried in noise, which also illustrated the weakness of the three-signal method when more than one coherent signal is present. Nance[31,32] repeated/validated this simulation as well as considered the cases where three and four coherent signals were buried in noise and found that the situation became progressively worse as the number of coherent sources increased. In addition, Nance[31,32] carried out a carefully-controlled model-scale experiment in an anechoic facility. Two electro-acoustic drivers were used to generate the coherent signals buried in uncorrelated noise produced by a jet flow. Fig. 6.3 in Nance[32] shows that when the coherent-signal separation is large (20 dB), the three-signal method provides a good estimate of the stronger signal. As the separation is reduced to 10 dB, the three-signal method gives a result that is within ± 3 dB for most frequencies. As the separation is further reduced (5 dB), the three-signal method begins to fail. A meaningful result is not obtained at 0 dB separation. These results are in full agreement with the conclusions of Minami and Ahuja.[30]

4.3 *Four-Signal-Coherence Method*

This subsection introduces a new coherence method for the determination of the far-field combustor noise. The gist of the method is to provide a better spectral estimate for the part of the pressure fluctuations in the combustor that actually propagates further downstream inside the engine, $G_{u_1u_1}(f)$. Rather than, as in the two-signal method, approximating it by the total combustor signature, $G_{11}(f)$, the three engine-internal sensors in the flow path are used for this purpose.

Combining the three-signal result, Eq. (4), for the coherent auto-spectrum at the combustor sensor CIP1 with Eq. (1), produces

$$G^{(4s)}_{u_4u_4}(f) = G^{(4s)}_{123-4}(f) = \frac{|G_{14}(f)|^2|G_{23}(f)|}{|G_{12}(f)||G_{13}(f)|} = \frac{\gamma^2_{14}(f)\gamma_{23}(f)}{\gamma_{12}(f)\gamma_{13}(f)}G_{44}(f)\,, \tag{7}$$

which here is referred to as the four-signal-method result for the far-field coherent combustor noise. The sensor configuration is labeled as 123-4 following the notational conventions introduced above for the two- and three-signal methods.

4.4 *Implementation*

A few details in regards to the calculations are briefly presented here, such as the need to compensate for the time delay between engine-internal and far-field sensors, the effects of having only finite time histories, the windowing and segment overlap used in the spectral analysis, and various criteria that the results must not violate, etc.

The signals $s_i(t)$, $i = 4,5,6$, must be time shifted to account for the physical propagation-time delay between the engine-internal sensors and the far-field microphones when signals from both sets are utilized. Following Miles,[33] the far-field microphone time series are shifted by 5800 points, which corresponds to an 88.5 ms time delay. The differences between the physical propagation time from each of the engine-internal sensors to the engine exit are sufficiently small (1 ms, or less) compared to the data segment length used herein (125 ms) and can be ignored. In a

sense, only the travel time from an 'average' engine-internal-sensor location to the far-field microphone need to be accounted for.

Theoretically, the coherence, $\gamma_{\alpha\beta}(f)$, between two signals, $\alpha(t)$ and $\beta(t)$, ranges from zero to unity. A value of zero at a particular frequency indicates that the two signals are uncorrelated, while a value of unity signifies that they are perfectly correlated. However, the time series used in practice are finite. Consequently, the computed value for the coherence will never be zero even for completely uncorrelated signals.[34] Instead, a coherence threshold value, ε, is calculated from[35]

$$\varepsilon^2 = 1 - (1-P)^{1/(N_s-1)}, \tag{8}$$

where $0 \le P \le 1$ is the confidence interval and N_s is the number of independent data segments used in estimating the coherence. If the computed coherence falls below this value at certain frequencies then the two signals are uncorrelated at those frequencies with a confidence level of P. $P = 0.95$ is used throughout the current investigation.

Welch[36] showed, in the context of estimating auto power spectra, that N_s can be replaced by $9M/11$ for 50-percent-overlapped segments, where M is the number of segments. Miles[35] suggested that a better estimate for the coherence threshold value, or noise floor, ε can be obtained by purposely unaligning the two time series. That is, a time delay is deliberately introduced to ensure that the two resulting finite time series are uncorrelated. The estimated unaligned coherence does not depend on any particular assumptions about the underlying statistical properties of the time series and accounts for any data-segment overlap and algorithms used in the analysis. The unaligned result captures the coherence of any discrete tones present in the signals and also provides an estimate of the minimum observable broadband coherence. Miles[33,35] found that Eq. (8) with $N_s = M$ provides a good estimate of the noise floor and this simplification is adopted here. Table 1 shows the number of data segments and resulting coherence threshold limit for various overlap settings in the present investigation. If the estimated coherence exceeds the threshold, the two time series contains coupled signals. If it is less than the threshold, the signals are random and appear independent for that particular number of samples/segments. Since the acoustic data records used here are sufficiently long, no significant difference in the results was observed when using different data-segment overlaps in the current study. Consequently, only results with zero percent overlap are presented herein.

Table 1. Coherence thresholds

$P = 0.95$		
overlap, %	M	ε
0	559	0.0732
25	745	0.0634
50	1118	0.0518

In the two-signal (coherent-output-power) method calculations carried out here, the estimated coherence is replaced by the threshold value ε if it falls below that value for a particular narrow-band frequency. That is, the estimated narrow-band combustor-noise component, say $G_{u_4u_4}(f)$, is simply set to $\varepsilon^2 G_{44}(f)$ for the frequency in question. Otherwise it is given by (2).

Mathematically, it follows that

$$\varepsilon^2 < \gamma_{\alpha\iota}\gamma_{\beta\iota}/\gamma_{\alpha\beta} < \varepsilon^{-1}. \tag{9}$$

The upper limit of this inequality is an unphysical result in view of Eqs. (4)–(6) and the fact that the combustor-noise component cannot exceed the total signal. Clearly, an additional discriminator is needed to ensure a physically realistic three-signal combustor-noise estimate. This is provided by the following necessary condition[24] for Eq. (4) to be valid:

$$\Theta \equiv \arg(G_{21}G_{31}^*/G_{23}) = \arg(G_{12}^*G_{13}/G_{23}) = 0. \tag{10}$$

The standard deviation (in radians) of the estimate for the cross-spectrum phase angle $\theta_{\alpha\beta} = \arg(G_{\alpha\beta})$ is given by[8,33]

$$\sigma_{\alpha\beta} = \sin^{-1}\sqrt{[1/\max(\gamma_{\alpha\beta}^2, \varepsilon^2) - 1]/2N_s}, \tag{11}$$

where the coherence threshold value, ε, explicitly has been added here to the formula. Note that the standard deviation is zero for perfectly correlated signals and increases as the coherence is diminished. Consequently, in the three-signal method calculations carried out here, the estimated narrowband combustor-noise component for a particular narrowband frequency, say $G_{u_1u_1}(f)$, is set to $\varepsilon^2 G_{11}(f)$ if any of the estimated coherence values, γ_{12}, γ_{13}, or γ_{23}, fall below the threshold value ε, or if the estimated phase angle $\Theta > \sigma_{12} + \sigma_{13} + \sigma_{23}$; otherwise it is given by (4).

4.5 *Statistical Uncertainty*

The textbook by Bendat and Piersol[8] gives a summary of statistical random error formulas for single input/output systems. From these, it follows[24] that the statistical uncertainties of the two-signal-method estimates, for the 1-4

configuration, are given by

$$\mathscr{E}_r[G_{44}(f)] = \frac{1}{\sqrt{N_s}}\,, \tag{12a}$$

$$\mathscr{E}_r[G_{14}(f)] = \frac{1}{\gamma_{14}(f)\sqrt{N_s}}\,, \tag{12b}$$

$$\mathscr{E}_r[\gamma^2_{14}(f)] = \frac{\sqrt{2}[1-\gamma^2_{14}(f)]}{\gamma_{14}(f)\sqrt{N_s}}\,, \tag{12c}$$

$$\mathscr{E}_r[G^{(2s)}_{1-4}(f)] = \frac{[2-\gamma^2_{14}(f)]^{1/2}}{\gamma_{14}(f)\sqrt{N_s}}\,, \quad \text{if} \quad G_{n_1n_1}(f) = 0\,, \tag{12d}$$

where $\mathscr{E}_r$ denotes the relative error/uncertainty. Equations (12a) and (12c) are the well-known results that the uncertainty in an auto-spectrum estimation decreases as the inverse square root of the number averages used and that, since coherence uncertainty vanishes as the signals become correlated, the computed coherence values are more accurate than the quantities used in its evaluation. The estimate (12d) is for the idealized situation when the input signal (see Fig. 4) does not contain a noise component. Consequently, it does not reflect the inherent bias error of the two-signal coherence method, which can be a significant issue[24] for real engine data. Furthermore, Eq. (12a) shows that for the present computations without overlap of data-segments, the statistical uncertainty of the total-noise auto spectrum is 4.2 percent, which is about an order of magnitude smaller than the 33 percent (1.25 dB[22]) estimated measurement uncertainty.

Using logarithmic differencing, it follows that the statistical uncertainty in the three- and four-signal methods, for the 12-4 and 123-4 configurations respectively, can be expressed as

$$\mathscr{E}_r[G^{(3s)}_{12-4}(f)] \le \tfrac{1}{2}\left\{\mathscr{E}_r[\gamma^2_{12}(f)] + \mathscr{E}_r[\gamma^2_{14}(f)] + \mathscr{E}_r[\gamma^2_{24}(f)]\right\} + \mathscr{E}_r[G_{44}(f)]\,. \tag{13}$$

$$\mathscr{E}_r[G^{(4s)}_{123-4}(f)] \le \tfrac{1}{2}\left\{\mathscr{E}_r[\gamma^2_{12}(f)] + \mathscr{E}_r[\gamma^2_{13}(f)] + 2\mathscr{E}_r[\gamma^2_{14}(f)] + \mathscr{E}_r[\gamma^2_{23}(f)]\right\} + \mathscr{E}_r[G_{44}(f)]\,. \tag{14}$$

For perfectly correlated signals, Eqs. (12d)–(14) reduce to the equivalent of Eq. (12a). As the signals become uncorrelated, Eqs. (12d)–(14) indicate a relative uncertainty of $\sqrt{2/\varepsilon^2 N_s}$, $\frac{3}{2}\sqrt{2/\varepsilon^2 N_s}$, and $\frac{5}{2}\sqrt{2/\varepsilon^2 N_s}$, respectively. Using the present number of non-overlapping data segments ($N_s = 559$, $\varepsilon^2 = 0.0732$), the statistical uncertainty in the combustor-noise estimate is about 4 percent when the signals are highly correlated and could roughly become as high as 80, 120, and 200 percent (depending on source-separation method) as they become poorly correlated. This suggests that the three- and four-signal methods are successively less robust as compared to the two-signal method when the coherence is small.

Nance[31,32] attempted to determine the uncertainty in the three-signal source-separation method using a root-sum-square procedure as outlined in Chapters 2–4 in Coleman and Steele.[37] However, this method assumes that the uncertainty (random and systematic) in a variable is uncorrelated to those of the other variables, such as would be the case if each variable corresponds to a distinct measured quantity. This is not the case in his work[31,32] since the approach starts from existing and well-established[8,38,39] uncertainty results for spectral estimation, see Table 9.1 in Nance,[32] and these are then used to provide uncertainties for the three-signal and two-signal methods. The fallacy of this approach can be directly seen by comparing Eq. 9.37 in Nance[32] for the uncertainty in the coherent-output method with the correct result[8] in Eq. (12d). The first and third term inside the square-root bracket on the right-hand side of his equation are systematic-uncertainty terms, and can for the present purpose be set to zero. The resulting estimate can easily be shown to be smaller than the correct value. The reason for this discrepancy is simply that both the mean-square coherence and the auto-spectrum depend on the measured signal at the observation location and, consequently, the uncertainties in these two computed variables are not uncorrelated. The uncertainty analysis by Nance[31,32] for the three-signal method also violates the basic assumption of the root-sum-square procedure and, hence, is incorrect.

5 Results

This section presents results for the coherent combustor-noise component of the total noise signature at the 130^o far-field-microphone location obtained by using the two-signal, three-signal, and the new four-signal coherence methods. A zero percent data-segment overlap was used in all computations in this section. Results are presented for the

static-engine-test operational conditions of 48, 60, 71, and 87 percent corrected fan speed. These set points correspond to flight idle and the certification points of approach, flyover, and sideline.

5.1 *Two-Signal Method*

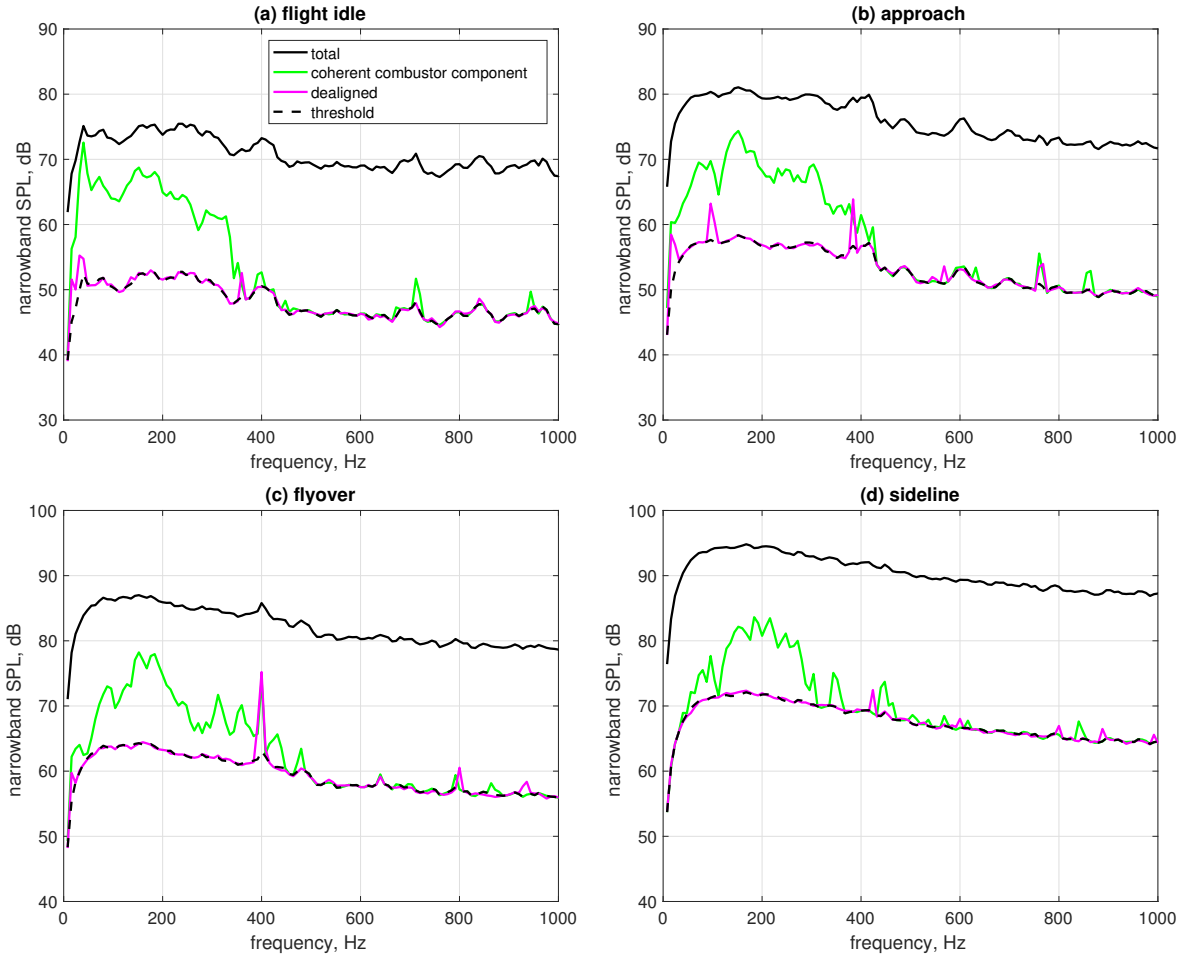

Figure 5. Far-field total and combustor-noise narrowband (8 Hz) SPL versus frequency in the 130^o direction at flight idle (a), approach (b), flyover (c), and sideline (d) conditions; solid black curves—total noise signature; dashed black curves—threshold level; green and magenta curves—aligned and purposely dealigned combustor-noise component using combustor sensor and far-field microphone

Figure 5 shows the far-field narrowband (8 Hz) SPL results obtained by applying the two-signal source-separation procedure to the time series from the CIP1 combustor sensor and the 130^o microphone, sensors 1 and 4 in Fig. 4. Panels (a) – (d) correspond to the flight-idle, approach, flyover, and sideline conditions, respectively. The solid and dashed black curves show the total noise signature G_{44} and the threshold value $\varepsilon^2 G_{44}$ for the coherent combustor-noise component. The green and magenta curves in these panels represent the coherent combustor-noise component at the far-field location, $G_{1-4}^{(2s)}$. The green curves show the case where the signals are properly aligned to account for the travel time between the two sensors. The magenta curves illustrate the case where the far-field microphone time series is shifted by 16500 points, which corresponds to a 251.8 ms time delay, to purposely decorrelate any broadband component present in the signals. Recall that computed coherent-output-power values lower than the threshold are not significant and, consequently, are not plotted here. The figure indicates that broadband combustor noise is present up

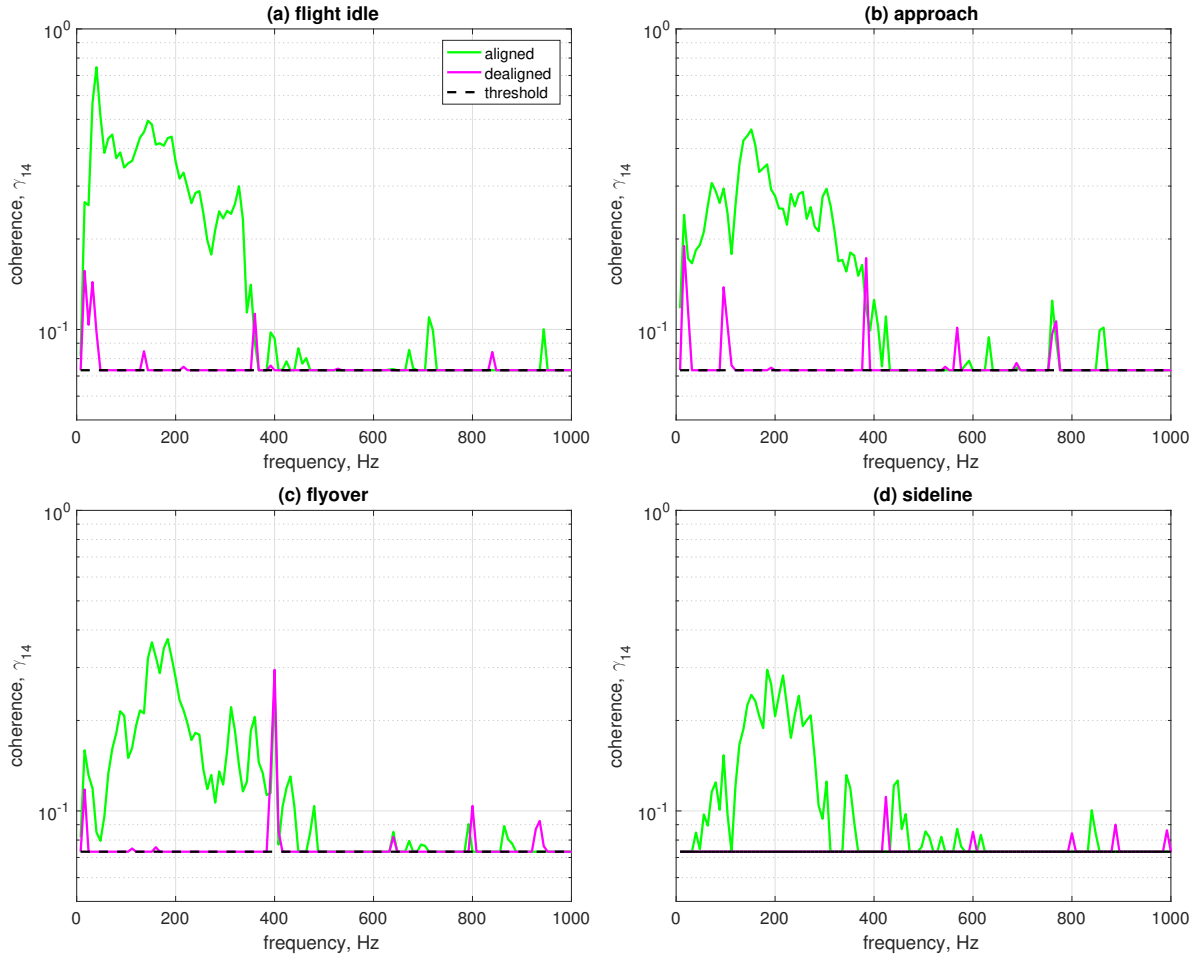

Figure 6. Far-field narrow-band (8 Hz) combustor-noise coherence in the 130^o direction determined using combustor sensor and farfield microphone at flight idle (a), approach (b), flyover (c), and sideline (d) conditions; green curves—aligned signals; magenta curves—dealigned signals; dashed black line—threshold level

to about 450 Hz. The results in panels (a) and (b) compare well with previously published results by Hultgren and Miles,[24] which were computed with a 50 percent overlap of the data segments. Results corresponding to panel (a) can be found in their Figs. 4(a) and 5. Their Fig. 6(a) presents results corresponding to panel (b) here. No significant differences between the current and previous results can be identified.

Figure 6 shows the corresponding narrowband coherence values for the cases presented in Fig. 5. The green and magenta curves also here indicate perfectly aligned and deliberately unaligned signals. Computed coherence values below the statistical threshold are not shown. The aligned results in this figure indicates that broadband combustor noise is present at the far-field location for frequencies up to about 450 Hz. The unaligned results show the presence of discrete tones originating in combustor, or earlier in the core flow path, in the same frequency range.

Figure 7 shows the far-field narrowband (8 Hz) SPL results obtained by applying the two-signal source-separation procedure to the time series from the CIP1 combustor sensor, the turbine-exit sensors T551 and T552, each in turn, together with the 130^o microphone, i.e. by using sensor configurations 1-4, 2-4, and 3-4. Panels (a) – (d) correspond to the flight-idle, approach, flyover, and sideline conditions, respectively. The solid and dashed black curves show the total noise signature G_{44} and the threshold value $\varepsilon^2 G_{44}$ for the coherent combustor-noise component. The green, blue, and cyan symbols in these panels represent the coherent combustor-noise-component estimates at the far-field location, $G^{(2s)}_{1-4}$, $G^{(2s)}_{2-4}$, and $G^{(2s)}_{3-4}$, respectively. The choice was made from here on to use symbols rather than continuous lines

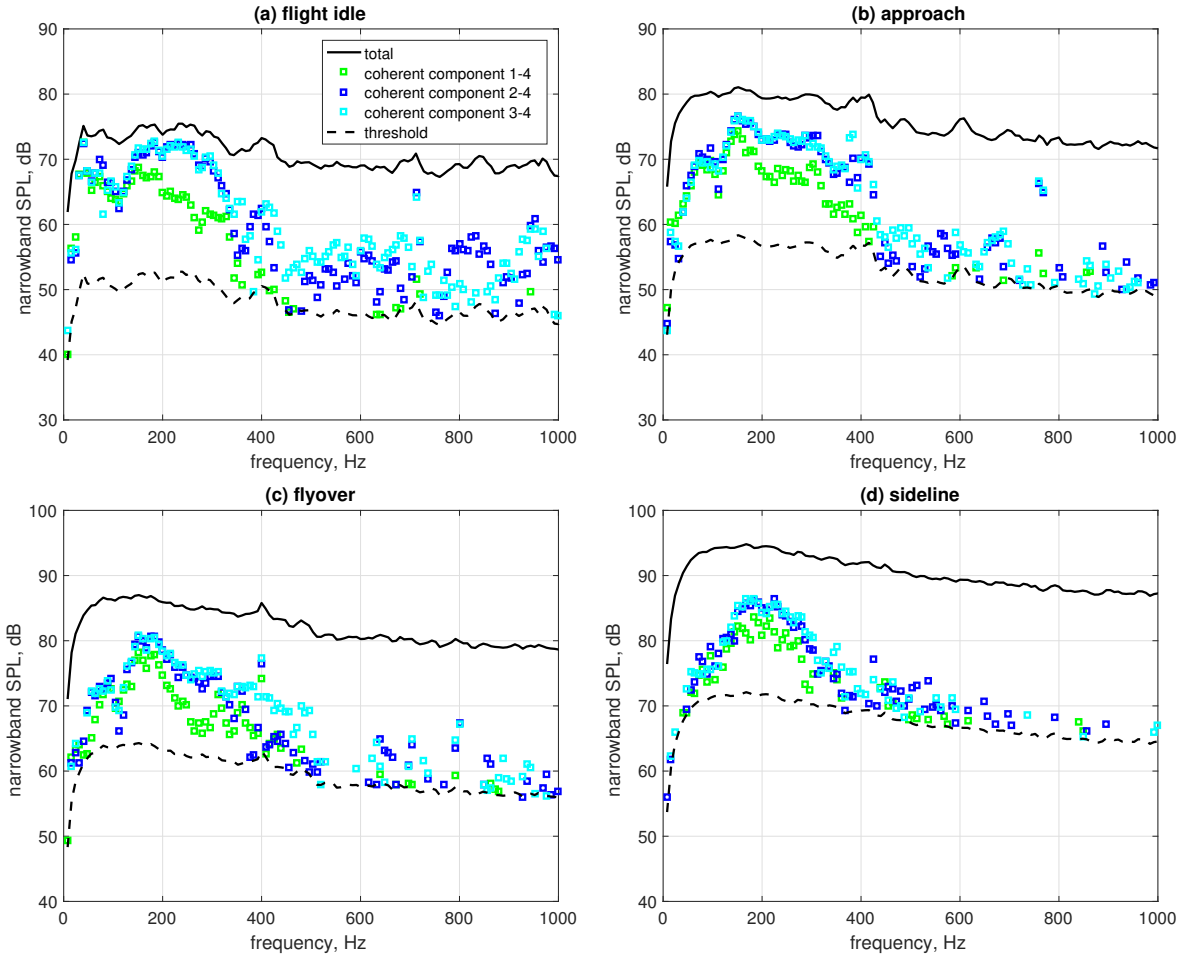

Figure 7. Far-field total and combustor-noise narrowband (8 Hz) SPL versus frequency in the 130^o direction at flight idle (a), approach (b), flyover (c), and sideline (d) conditions; solid and dashed black curves—total noise signature and threshold level; green, blue, and magenta symbols—combustor-noise component using sensors 1-4, 2-4, and 3-4, see Fig. 4

for the source-separation results so as to not clutter the plots with near vertical lines at frequencies where the 'raw' computed values fall below the threshold (or violate any other criteria). The 2-4 two-signal results (blue symbols) in panels (a) and (b) also agree well with the results presented in Figs. 5(a) and 6(b) in Hultgren and Miles.[24] It is clear also from this figure that broadband combustor noise is present at least up to about 450 Hz. Assuming that only broadband noise originating in the combustor is present in this frequency range at the turbine exit, it is evident that the inherent positive-bias error in the two-signal methods leads to an underprediction of the peak value for the 1-4 implementation of the technique. The results obtained for the 2-4 and 3-4 configurations, that involve a turbine-exit sensor in addition to the far-field microphone, shown as blue and cyan symbols in this figure, also indicate the presence of coherent broadband noise, as well as tones, for frequencies larger than about 450 Hz, see also Hultgren and Miles[24] Fig 5. Even though the exact source of this broadband noise is not clear, it is most likely associated with the turbine.

The results in Fig. 7(b) are in general agreement with the ones presented by Mendoza et al.[23] in their Fig. 12(b). The red circles and blue triangles in their figure correspond to configurations 1-4 and 2-4, respectively. There is good agreement between the present results and theirs for both the frequency range and levels of the estimated broadband combustion noise.

The narrowband results associated with Fig. 7 can be summed up and assigned to the appropriate 1/3-octave frequency band and this produces the 1/3-octave-SPL results shown in Figure 8 for the 1/3-octave center frequency range of 20 to 1000 Hz. The black squares represent the total noise signature G_{44} and the dashed line indicates the

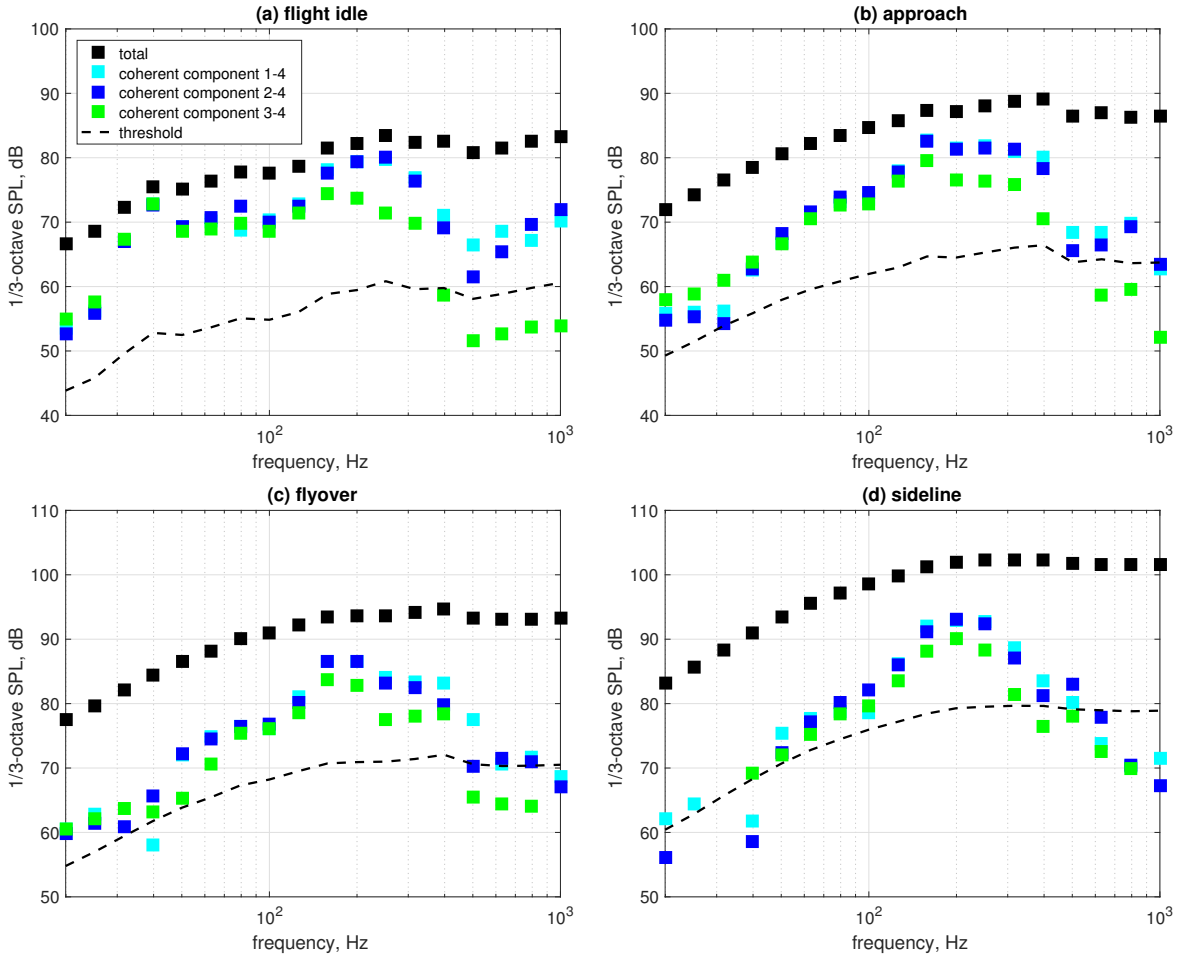

Figure 8. Far-field total and combustor-noise 1/3-octave SPL versus 1/3-octave center frequency in the 130^o direction at flight idle (a), approach (b), flyover (c), and sideline (d) conditions; solid black symbols—total noise signature; green, blue, and magenta symbols—combustor-noise component using sensors 1-4, 2-4, and 3-4, see Fig. 4; dashed black line—threshold level

threshold value for the coherent combustor component. Any educed combustor-noise result below the threshold line is not meaningful using the present number of data segments. The green, blue, and cyan squares correspond to the combustion noise detected using the present three two-signal configurations 1-4, 2-4, and 3-4, respectively. The 1-4 and 2-4 results agree well with the corresponding results in Fig. 3 in Hultgren and Miles.[24] In their study, the combustor-noise 1/3-octave SPL value was set to the threshold value if the latter exceeded the former, whereas this was not done here for 1/3-octave results.

5.2 *Three-Signal Method*

Figure 9 shows the far-field narrowband (8 Hz) SPL results obtained by applying the three-signal source-separation procedure to the three possible permutations using time series from two of the internal sensors, CIP1, T551 and T552, in combination with the 130^o microphone, i.e. the 12-4, 13-4, and 23-4 configurations. Panels (a) – (d) correspond to the flight-idle, approach, flyover, and sideline conditions, respectively. The solid and dashed black curves show the total noise signature G_{44} and the threshold value $\varepsilon^2 G_{44}$ for the coherent combustor-noise component. The blue, cyan, and magenta symbols in these panels represent the coherent combustor-noise-component estimates at the far-field location, $G^{(3s)}_{12-4}$, $G^{(3s)}_{13-4}$, and $G^{(3s)}_{23-4}$, respectively. Note that any raw coherent-combustor-noise estimate that violates the criteria in Section 4.4 has been rejected and is not shown in this figure. The results from all three configurations

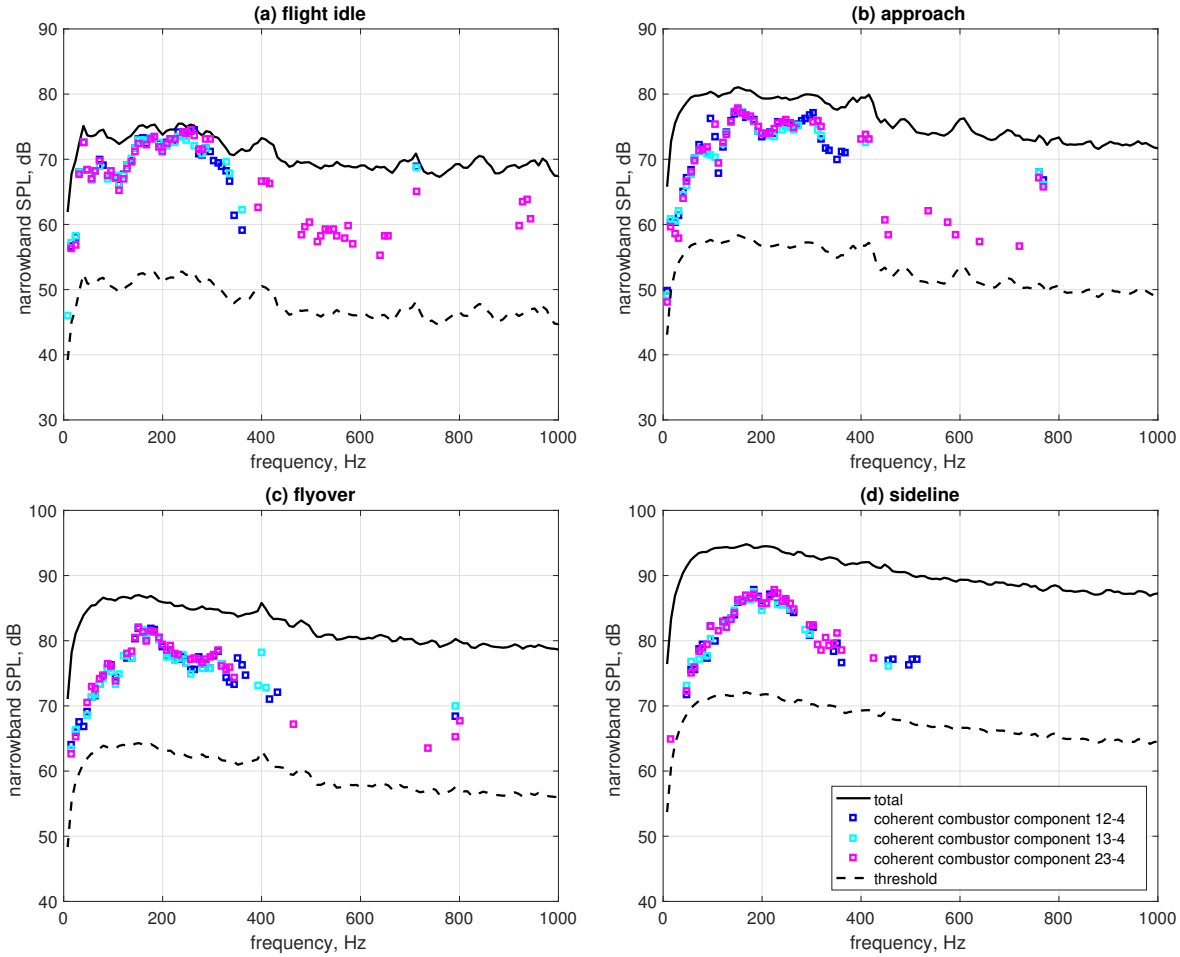

Figure 9. Far-field total and combustor-noise narrowband (8 Hz) SPL versus frequency in the 130^o direction at flight idle (a), approach (b), flyover (c), and sideline (d) conditions; solid and dashed black curves—total noise signature and threshold level; blue, cyan, and magenta symbols—combustor-noise component using combustor sensors 12-4, 13-4, and 23-4, see Fig. 4

indicate that there is coherent broadband combustor noise present at the far-field location for frequencies up to about 350 Hz. This is in agreement with the 12-4 configuration results, computed with 50 percent data segment overlap, in Hultgren and Miles [24] for the flight-idle and approach conditions, see their Figs. 4(c), 5(a), and 6(c). Panels (c) and (d) in their Fig. 4 also illustrate the raw uncorrected three-signal 12-4 result for the coherent combustor-noise component and the phase-angle tolerance corresponding to Eq. (10) for the lowest power setting. Their Figs. 5(b) and 6(c) also show the deliberately unaligned three-signal results for the flight-idle and approach conditions.

There is also a reasonable agreement between the present 23-4 results in Fig. 9(b) and the corresponding results shown by Mendoza et al. [23] in their Fig. 13(b) using orange 'plus' symbols. They refer to that result as a partial coherence result, labeled PCM SPLu. As can be seen from their Eq. (2), it involves only three sensors and directly corresponds to $G^{(3s)}_{23-4}$ when using the present sensor numbering convention. There is a reasonable agreement for frequencies up to about 350 Hz, with some deviation at higher frequencies.

The two-signal results in the previous subsection indicated the presence of broadband combustor noise also in the 350–450 Hz range. The reason that the three-signal methods fail to detect broadband noise in this frequency range is likely due to the lower levels of coherence there. As already discussed, the three-signal method becomes less robust as the coherence decreases. The magenta symbols (23-4 configuration) in Fig. 5 indicates the presence of coherent engine-internal noise at the far-field location also for frequencies larger than about 450 Hz, just as was the case for

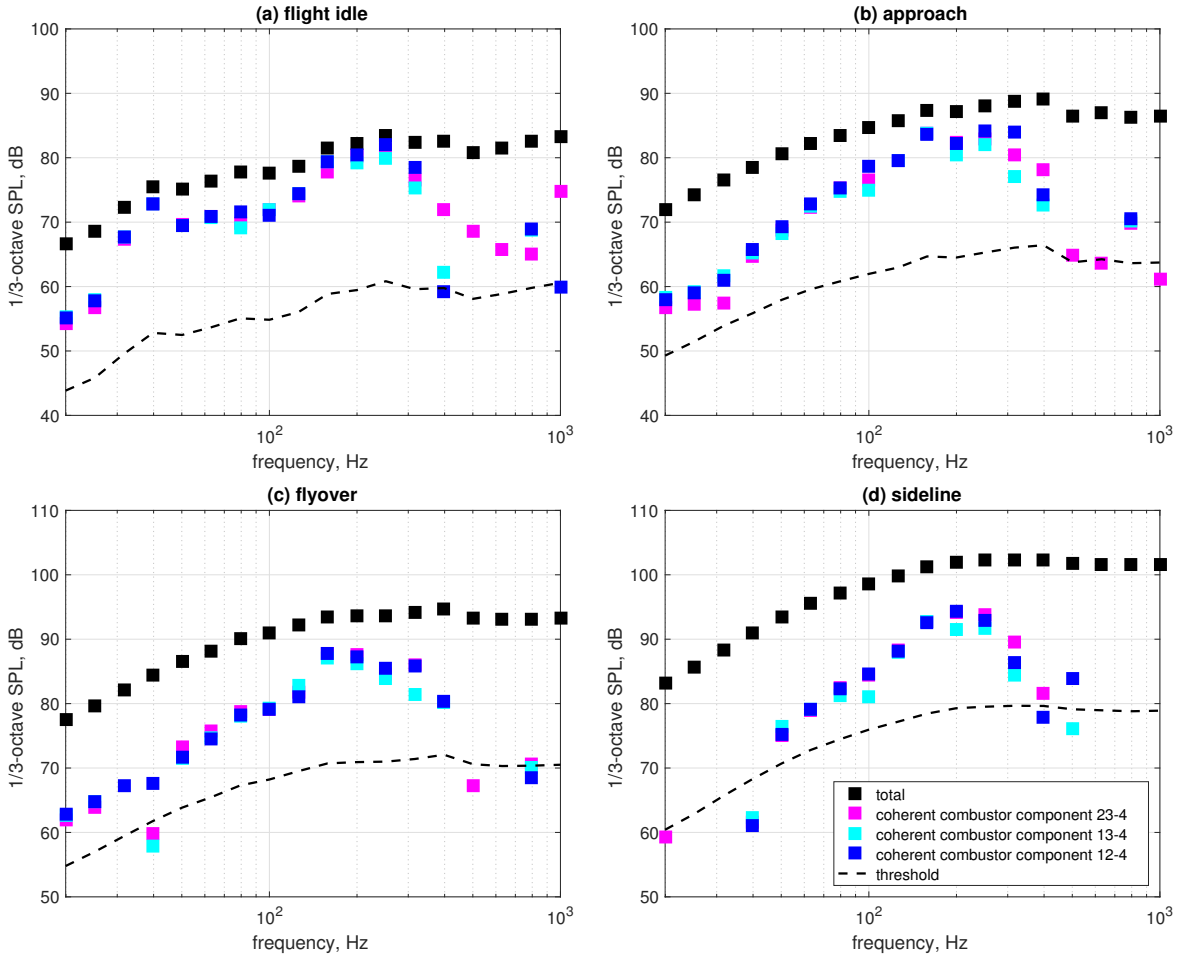

Figure 10. Far-field total and combustor-noise 1/3-octave SPL versus 1/3-octave center frequency in the 130^o direction at flight idle (a), approach (b), flyover (c), and sideline (d) conditions; solid black symbols—total noise signature; blue, cyan, and magenta symbols—combustor-noise component using sensors 12-4, 13-4, and 23-4, see Fig. 4; dashed black line—threshold level

the 2-4 and 3-4 two-signal configurations. This is particularly so at the flight-idle condition, but also at the approach condition, for the three-signal result. Again, the source of this noise is most likely not associated with the combustor.

Figure 10 depicts the results shown in Fig. 9, but plotted on a 1/3-octave basis. The operational conditions are the same and the same color legend is used. The black squares represent the total noise signature G_{44} and the dashed line indicates the threshold value for the computed coherent combustor component to be meaningful for the present number of available independent data segments. The blue, cyan, and magenta squares correspond to the coherent noise detected using the present three three-signal configurations 12-4, 13-4, and 23-4. The blue symbols, 12-4 configuration, agree well with the corresponding results in Fig. 3 of Hultgren and Miles [24] showing again that the choice of data-segment overlap in the computations does not significantly affect the results.

The three configurations yield very similar results when a significant combustor noise component is detected by the three-signal method, i.e. for 1/3-octave frequency bands less than 400 Hz. The 23-4 configuration also yields a significant coherent component in the 400 to 800 Hz 1/3-octave center-frequency range, but only for the flight-idle condition. Since this configuration does not involve any sensor inside the combustor and since the configurations that do fail to detect any coherent component in this frequency range, it follows that this component has its origin in the engine core, but downstream of the combustor.

5.3 *Four-Signal Method*

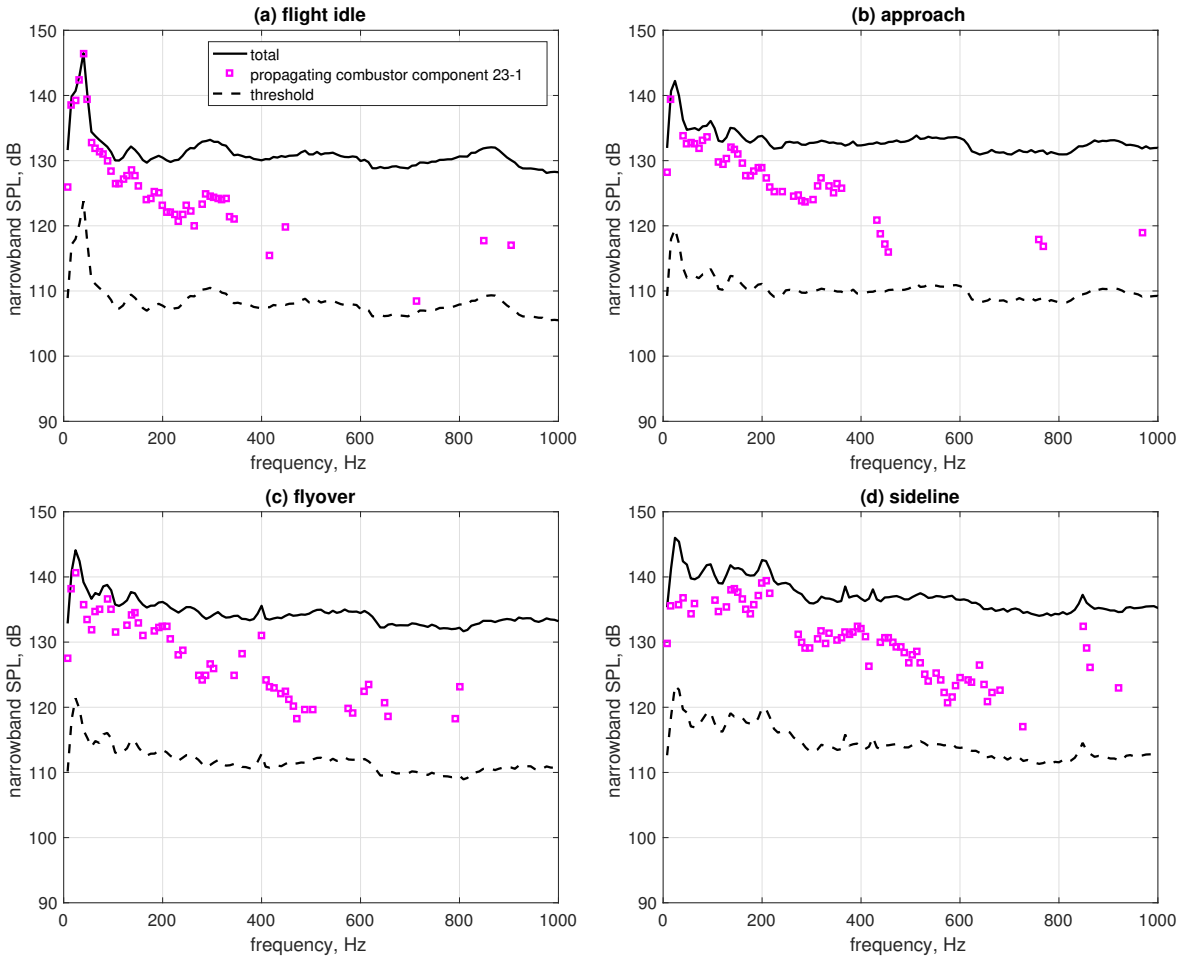

Figure 11. Narrowband (8 Hz) SPL versus frequency for the combustor total pressure fluctuation and propagating combustor-noise component at the combustor internal sensor CIP1 for flight idle (a), approach (b), flyover (c), and sideline (d) conditions; solid and dashed black curves—total unsteady pressure and threshold level; magenta symbols—combustor-noise component using engine-internal sensors 23-1, see Fig. 4

5.3.1 ***Combustor-sensor location*** The implicit first step in implementing the new four-signal method, Eq. (7), is to determine the part of the overall unsteady pressure fluctuation in the combustor that actually propagates further downstream in the engine interior. This is accomplished by using the three-signal estimate provided by Eq. (4). Figures 11 and 12 show the results from applying this evaluation on a narrowband and 1/3-octave basis, respectively, for the four operating conditions under consideration here: flight idle, approach, flyover, and sideline—panels (a)–(d). The black curves and symbols represent the SPL of the total unsteady pressure fluctuation at the combustor-sensor location. The computed SPL values for the propagating component, that do not violate the criteria in Section 4.4, are plotted using magenta symbols. The dashed black curves show the threshold level for the source-separation method—any computed value below this level is not significant. Figure 13 shows the corresponding three-signal method narrowband phase angle, Eq. (10), again using magenta symbols for results that pass all validation criteria. The solid orange curves depict the raw phase-angle results and the solid black curves show the phase-angle tolerance. From these figures, it follows that the total unsteady pressure signature is only dominated by the propagating combustor noise component for frequencies less than about 200 Hz, with the relative strength decreasing with increasing engine

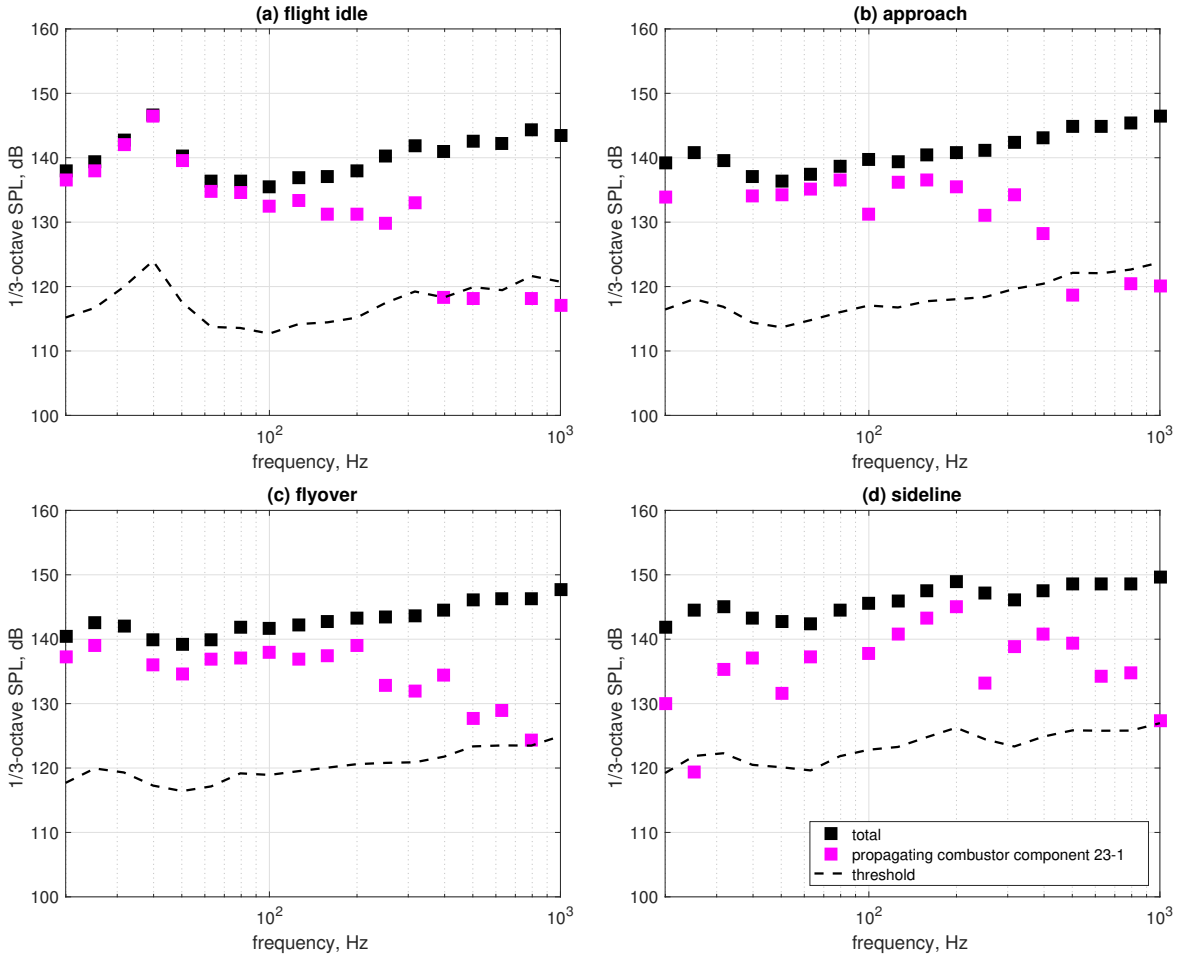

Figure 12. 1/3-octave SPL versus 1/3-octave-band center frequency for the combustor total pressure fluctuation and propagating combustor-noise component at the combustor internal sensor CIP1 for flight idle (a), approach (b), flyover (c), and sideline (d) conditions; solid black symbols—total unsteady pressure; magenta symbols—combustor-noise component using engine-internal sensors 23-1, see Fig. 4; dashed black lines—threshold level

power. However, the frequency range where the propagating component is significant appears to increase with the engine power level—up to about 350 Hz for the lowest set point and increasing to about 650 Hz at the highest power level. The decrease of the relative strength (i.e. $G^{(3s)}_{u_1u_1}$ compared to G_{11}) with increasing frequency illustrated here explains the bias error exhibited by the 1-4 two-signal-method results in Section 5.1.

5.3.2 ***Far-field-microphone location*** Figures 14 and 15 compare two-, three-, and the new four-signal far-field SPL results in the 130° direction, obtained using the 1-4, 12-4, and 123-4 sensor configurations, on a narrowband and 1/3-octave-band basis, respectively. The black curves and symbols represent the total noise signature, G_{44}, at the far-field location and the black dashed lines show the threshold value for the coherent combustor component, $\varepsilon^2 G_{44}$. The green, blue, and red symbols show the combustor-noise component educed using the sensor configurations 1-4, 12-4, 123-4, respectively.

Figure 14 shows that, for frequencies up to about 350 Hz, the three- and four-signal methods, 12-4 and 123-4 sensor configurations respectively, yield comparable results at all set points. For higher frequencies, the situation is less obvious. Clearly, the 'isolated' four-signal result in Fig. 14(a) at around 700 Hz is spurious since a noise component cannot exceed the total. Also, Fig. 11(a) shows that the detected propagating combustor-noise component

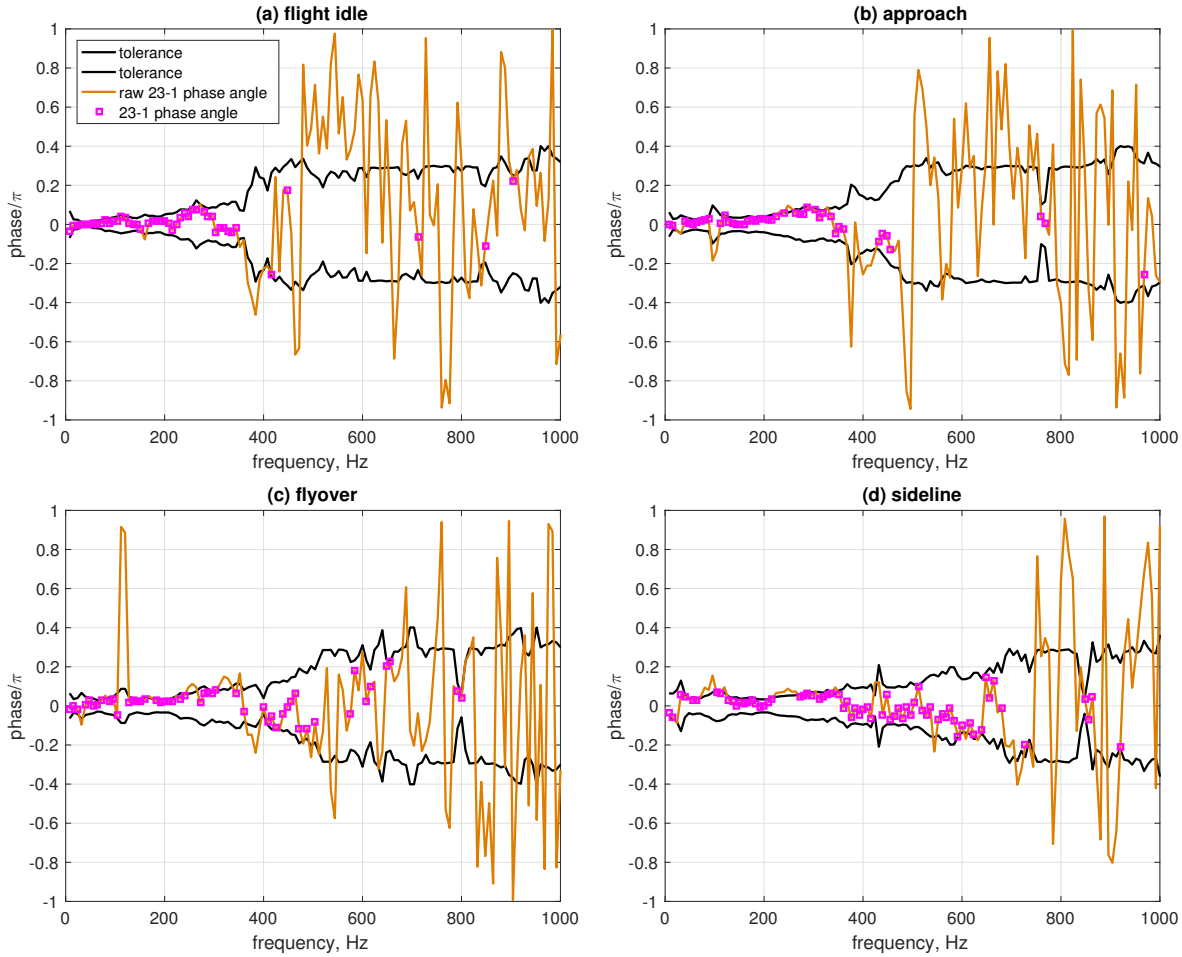

Figure 13. Narrowband (8 Hz) phase angle versus frequency for the three-signal estimation of the propagating combustor-noise component at the combustor internal sensor CIP1 for flight idle (a), approach (b), flyover (c), and sideline (d) conditions; magenta symbols—phase angle for three-signal method using engine-internal sensors 23-1, see Fig. 4; solid orange curves—corresponding raw phase angle; solid black curves—threshold value

at that frequency is barely above the threshold level, which explains the error/uncertainty in the corresponding four-signal result in the far field. Figures 14(c,d) indicate the presence of coherent broadband combustor noise up to about 500 Hz and 650 Hz for the flyover and sideline conditions, respectively. The large scatter in the four-signal results that are apparent in these two panels above 350 Hz can be explained by the diminishing levels of the coherent propagating component in the combustor, see Figs. 11(c,d), the increased uncertainty in the estimate of the latter which is exemplified by the phase result in Figs. 13(c,d), as well as the low coherence value, γ_{14}, between the combustor and far-field signals, see Fig. 6.

Nevertheless, the new four-signal method does indicate the presence of a coherent combustor-noise component at higher frequencies than in our previous work.[24] However, the method is not robust enough to produce a reliable estimate of the far-field coherent combustor-noise level at these higher frequencies on a narrowband basis. When summing up the narrowband results to produce the corresponding 1/3-octave results, it is likely that some, if not much, of these uncertainties will cancel (or filter) out thereby leading to a better estimate albeit on a cruder basis. This is borne out by the 1/3-octave results shown in Fig. 15. For the flight-idle and approach conditions, panels (a) and (b), the three- and four-signal methods essentially produce the same results with only a few exceptions. A coherent broadband combustor-noise component is seen for 1/3-octave band center frequencies up to 325 Hz. For the flyover and sideline conditions, panels (c) and (d), there are, in general, slightly more differences between the three- and

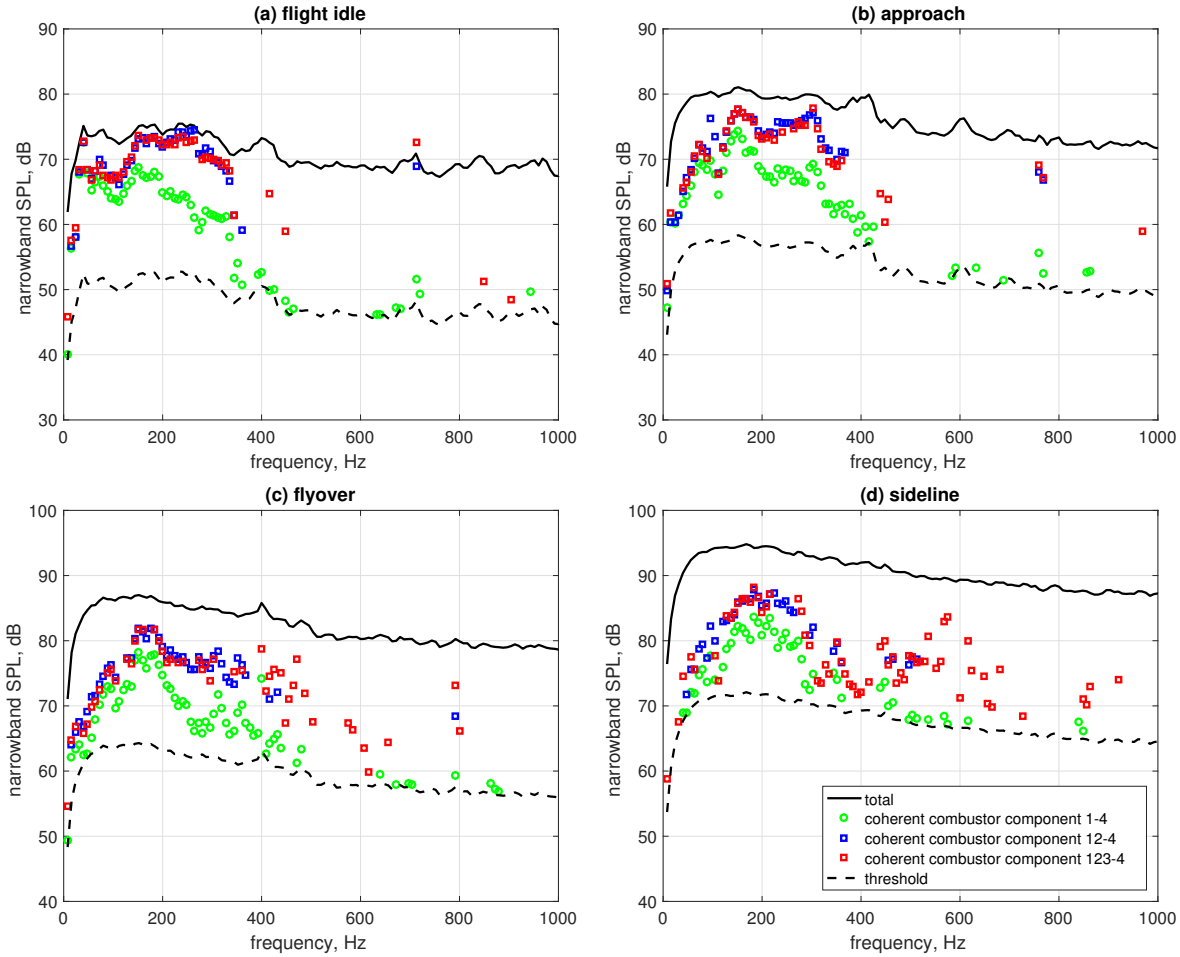

Figure 14. Far-field total and combustor-noise narrowband (8 Hz) SPL versus frequency in the 130^o direction at flight idle (a), approach (b), flyover (c), and sideline (d) conditions; solid and dashed black curves—total noise signature and threshold level; green, blue, and red symbols—combustor-noise component using combustor sensors 1-4, 12-4, and 123-4, see Fig. 4

four-signal results for center frequencies lesser or equal to 325 Hz as compared to the situation for two lowest-power set points. However, the four-signal results show coherent combustor broadband noise up to 500 Hz and 650 Hz for the flyover and sideline conditions, respectively.

6 Summary and Discussion

Direct measurement of far-field noise originating in the combustor is difficult during static engine tests due to the presence of other dominating noise sources. Coherence-based source-separation techniques, using engine-internal sensors as well as a far-field microphone, are needed to educe the combustor-noise component from the total engine-noise signature. In order to further evaluate such methods for combustor-noise investigations, all possible permutations of two- and three-signal methods involving engine-internal sensors were applied to existing acoustic data from Configuration 35 of the NASA/Honeywell EVNERT static-engine test program.[22] For two-signal methods, this means sensor combinations 1-4, 2-4, and 3-4, see Fig. 4. For three-signal methods this implies using sensor configurations 12-4, 13-4, and 23-4. In addition, a new four-signal method, involving sensor configuration 123-4, was proposed and tested.

Because the acoustic time histories from the EVNERT tests each contains over 4.5 million data points, a sufficiently large number of data segments is available for the averaging technique used in the data processing and no significant differences in representative results were observed when using different data-segment overlaps. Consequently,

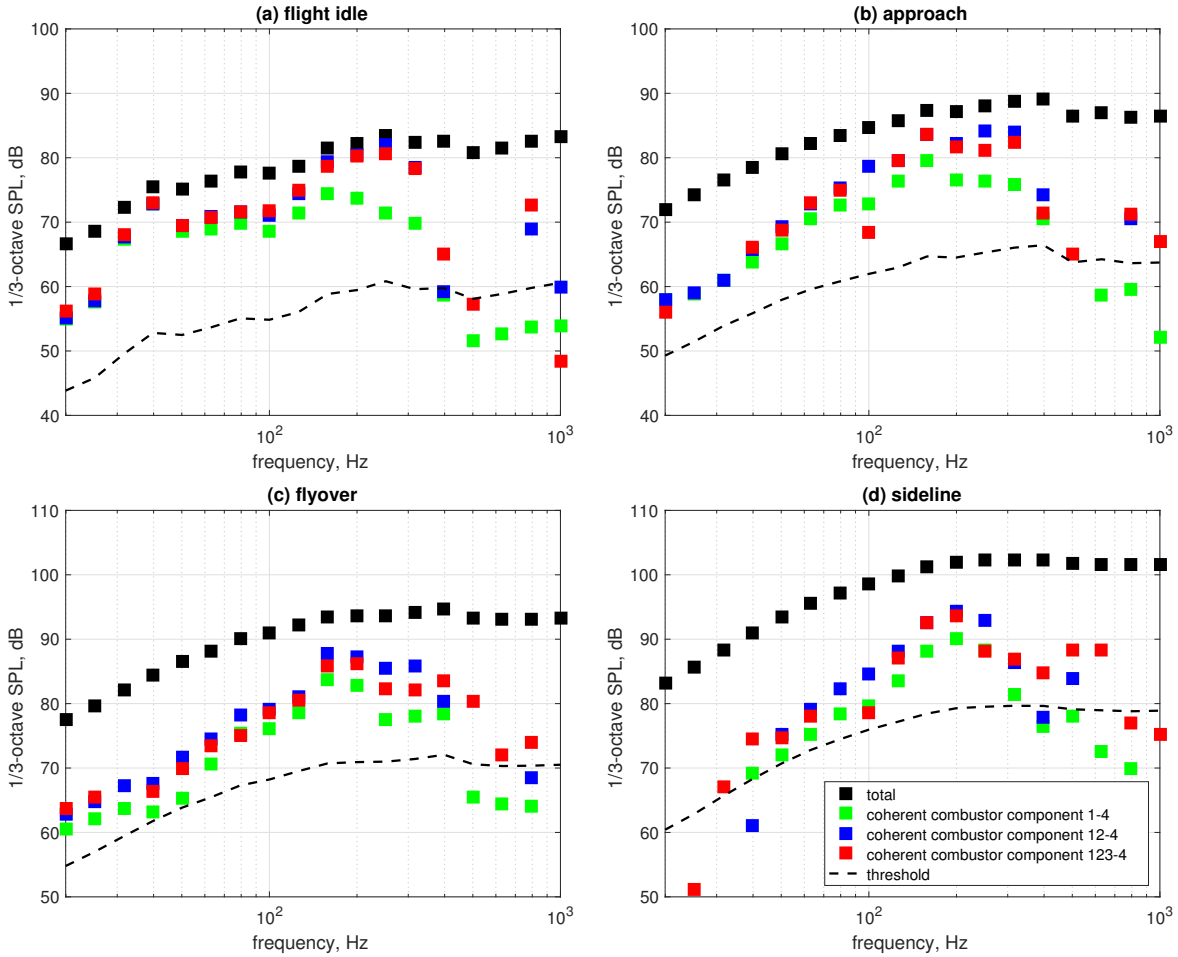

Figure 15. Far-field total and combustor-noise 1/3-octave SPL versus 1/3-octave center frequency in the 130^o direction at flight idle (a), approach (b), flyover (c), and sideline (d) conditions; solid black symbols—total noise signature; blue, cyan, and magenta symbols—combustor-noise component using sensors 1-4, 12-4, and 123-4, see Fig. 4; dashed black line—threshold level

the majority of the computations in this work, including all presented in this report, were carried out without using any data-segment overlap. The present results show good agreement with previously published investigations,[23,24] also using the EVNERT acoustic data, where 25 and 50 percent data-segment overlaps were used.

The two-signal method is quite robust, but has a bias error due to the neglected input noise signal and, consequently, underpredicts the true level of the coherent signal at the observer location. This is a significant issue for the 1-4 sensor configuration because of the presence in the combustor of hydrodynamic pressure fluctuations, as well as higher acoustic modes that are cut-off further downstream in the engine interior—neither of which are capable of reaching the far-field microphone location. This is less of an issue for the 2-4 and 3-4 configurations, which use one of the two engine-internal sensors at the turbine exit in combination with the far-field microphone. However, the two-signal method in either of these latter two configurations will also detect any other coherent broadband signal originating downstream of the combustor, but upstream of the turbine exit, such as turbine broadband noise. In theory, there should be a sufficient frequency separation between combustor- and turbine-broadband noise so that the different components of an educed coherent result can be discerned on that basis. It is not obvious that is always assured in practice, however.

On the other hand, the three-signal method does not have a bias error, but is sensitive to the presence of multiple coherent sources, i.e., when two (but not all three) of the noise signals are correlated. Consequently, the method fails to produce reliable results at frequencies where additional coherent signals are present, even when these are

weak compared to the coherent combustor noise signal,[30] and also as the coherence becomes small. In general, the three-signal method is less robust than the two-signal method as the coherence decreases. Just as the two-signal configurations 2-4 and 3-4, the three-signal configuration 23-4, that only uses engine-internal sensors at the turbine exit, detects broadband noise in the far-field at higher frequencies that likely is originated downstream of the combustor. This illustrates the limitation of relying only on engine-internal sensors that are located downstream of the combustor in the three-signal source-separation method. If available, it is best practice to include a sensor located inside the combustor in combination with an engine-internal sensor further downstream in the flow path (such as the turbine-exit sensor used here) and a far-field microphone for the detection of coherent combustor noise in the far field.

The idea behind the new four-signal method is to first use the three engine-internal sensors to provide a better estimate for the combustor-noise source level in the combustor. Second, the measured cross spectrum between the combustor sensor and the far-field microphone can then be used in combination with this estimate to determine the coherent combustor noise at the microphone location. In some aspects, this method is a combination of the two- and three-signal approaches. For narrowband frequencies up to about 350 Hz, the four-signal method produces comparable results to the three-signal technique at all of the investigated engine operational points. In contrast to the relevant three-signal configurations, the new four-signal method also shows the presence of coherent combustor noise at higher frequencies. There is considerable scatter in the narrowband results at these higher frequencies, however, that is judged to be caused by a lack of robustness with reduced coherence in the new method. Because this scatter is filtered out when summing up the results on an 1/3-octave basis, the latter results appear more robust, but should still be considered preliminary. The new four-signal method shows promise and further evaluation is warranted if and when new data becomes available. It is conceivable that a more robust four-signal result could have been obtained if a different arrangement of the engine-internal sensors had been available for use. In the present study the turbine-exit sensors (sensors 2 and 3, see Figs. 3 and 4) are located at different circumferential locations but at the same axial location. A preferred sensor placement would be one where the sensors are all located at different streamwise positions in the engine flow path. This could possibly minimize the influence of coherent turbine broadband noise, or any additional weak coherent signal, on the results.

The overall lesson to be learned from this study is that when working with real-engine acoustic test data, information from all relevant engine-internal sensors should be used in the analysis. The noise-source structure is very rich in a real-aero-engine situation, particularly when compared to a tightly controlled laboratory experiment. In addition, isolated noise sources, such as those associated with bleed valves, compressor disk tones, casing vibrations, etc. can also appear and disappear between engine builds.[22] There is no magic-bullet approach and having results obtained by using different coherence techniques, with each utilizing several possible configurations that maximize the use of engine-internal sensors, will provide a better basis for the engineering judgment needed when evaluating/assessing the results.

REFERENCES

[1] J. F. Groeneweg, T. G. Sofrin, E. J. Rice, and P. R. Gliebe. Turbomachinery noise. In H. H. Hubbard, editor, *Aeroacoustics of Fligh Vehicles: Theory and Practice*, volume 1, chapter 3, pages 151–209. NASA Reference Publication 1258, WRDC Technical Report 90-3052, 1991.

[2] R. J. Mahan and A. Karchmer. Combustion and core noise. In H. H. Hubbard, editor, *Aeroacoustics of Flight Vehicles: Theory and Practice*, volume 1, chapter 9, pages 483–517. NASA Reference Publication 1258, WRDC Technical Report 90-3052, 1991.

[3] H. H. Hubbard, editor. *Aeroacoustics of Fligh Vehicles: Theory and Practice, Volume 1 and 2*. NASA Reference Publication 1258, WRDC Technical Report 90-3052, 1991.

[4] L. S. Hultgren, J. H. Miles, and P. C. E. Jorgenson. Engine system and core noise. In M. D. Dahl, editor, *Assessment of NASA's Aircraft Noise Prediction Capability*, chapter 3, pages 35–62. NASA/TP-2012-215653, 2012.

[5] L. S. Hultgren. A comparison of combustor-noise models. Technical Report AIAA Paper 2012-2087 (NASA/TM-2012-217671), 18th AIAA/CEAS Aerocoustics Conference, Colorado Springs, Colorado, 2012.

[6] A. P. Dowling and Y. Mahmoudi. Combustion noise. *Proceedings of the Combustion Institute*, 35:65–100, 2015.

[7] M. Ihme. Combustion and core noise. *Annual Review of Fluid Mechanics*, 49, to be published January 2017.

[8] J. S. Bendat and A. G. Piersol. *Engineering Applications of Correlation and Spectral Analysis*. Wiley-Interscience, 1980.

[9] A. M. Karchmer and M. Reshotko. Core noise source diagnostics on a turbofan engine using correlation and coherence techniques. Technical Report NASA-TM-X-73535, NASA, 1976.

[10] M. Reshotko, A. M. Karchmer, P. F. Penko, and J. G. McArdle. Core noise measurements on a YF-102 turbofan engine. *J. Aircraft*, 14(7):611–612, 1977.

[11] A. M. Karchmer. Identification and measurement of combustion noise from a turbofan engine using correlation and coherence techniques. Technical Report NASA-TM-73747, NASA, 1977.

[12] A. M. Karchmer, M. Reshotko, and F. J. Montegani. Measurement of far-field combustion noise from a turbofan engine using coherence functions. Technical Report AIAA Paper 1977-1277 (NASA-TM-73748), 4th AIAA Aeroacoustics Conference, Atlanta, Georgia, 1977.

[13] M. Reshotko and A. M. Karchmer. Core noise measurements from a small, general aviation turbofan engine. Technical Report NASA-TM-81610, NASA, 1980.

[14] V. L. Doyle and M. T. Moore. Core noise investigation of the CF6-50 turbofan engine. Technical Report NASA-CR-159749, NASA, 1980.

[15] E. A. Krejsa. New technique for the direct measurement of core noise from aircraft engines. Technical Report AIAA Paper 1981-1587 (NASA-TM-82634), 17th AIAA/SAE/ASME Joint Propulsion Conference, Colorado Springs, Colorado, 1981.

[16] E. A. Krejsa. Application of 3-signal coherence to core noise transmission. Technical Report AIAA Paper 1983-0759 (NASA-TM-83333), 8th AIAA Aeroacoustics Conference, Atlanta, Georgia, 1983.

[17] E. A. Krejsa. Combustion noise from gas turbine aircraft engines measurement of far-field levels. Technical Report NASA-TM-88971, NASA, 1987.

[18] A. M. Karchmer. Acoustic modal analysis of a full scale annular combustor. Technical Report AIAA Paper 1983-0760 (NASA-TM-83334), 8th AIAA Aeroacoustics Conference, Atlanta, Georgia, 1983.

[19] J. H. Miles and E. A. Krejsa. Pressure transfer function of a JT15D nozzle due to acoustic and convected entropy fluctuations. *J. Acoustical Society of America*, 72(6):2008–2019, 1982.

[20] E. A. Krejsa and A. M. Karchmer. Acoustic modal analysis of the pressure field in the tailpipe of a turbofan engine. Technical Report NASA-TM-83387, NASA, 1983.

[21] J. H. Miles, C. A. Wasserbauer, and E. A. Krejsa. Cross spectra between temperature and pressure in a constant area duct downstream of a combustor. Technical Report AIAA Paper 1983-0762 (NASA-TM-83351), 8th AIAA Aeroacoustics Conference, Atlanta, Georgia, 1983.

[22] D. S. Weir. Engine validation of noise and emission reduction technology phase I. Technical Report NASA/CR-2008-215225, NASA, 2008. Honeywell Report No. 21-13843, Honeywell Aerospace, Phoenix, Arizona.

[23] J. M. Mendoza, D. K. Nance, and K. K. Ahuja. Source separation from multiple microphone measurements in the far field of a full scale aero engine. Technical Report AIAA Paper 2008-2809, 14th AIAA/CEAS Aeroacoustic Conference, Vancouver, British Columbia, 2008.

[24] L. S. Hultgren and J. H. Miles. Noise-source separation using internal and far-field sensors for a full-scale turbofan engine. Technical Report AIAA Paper 2009-3220 (NASA/TM-2009-215834), 15th AIAA/CEAS Aeroacoustic Conference, Miami, Florida, 2009.

[25] L. S. Hultgren. Full-scale turbofan-engine turbine-transfer function determination using three internal sensors. Technical Report AIAA Paper 2011-2912 (NASA/TM-2012-217252), 17th AIAA/CEAS Aeroacoustic Conference, Portland, Oregon, 2011.

[26] C. M. Royalty and B. Schuster. Noise from a turbofan engine without a fan from the engine validation of noise and emission reduction technology (EVNERT) program. Technical Report AIAA 2008-2810, 14th AIAA/CEAS Aeroacoustics Conference, Vancouver, British Columbia, 2008.

[27] J. Y. Chung. Rejection of flow noise using a coherence function method. *J. Acoustical Society of America*, 62 (2):388–395, 1977.

[28] J. S. Hsu and K. K. Ahuja. A coherence-based technique to separate internal mixing noise from farfield measurements. Technical Report AIAA Paper 1998-2296, 4th AIAA/CEAS Aeroacoustic Conference, Toulouse, France, 1998.

[29] B. N. Shivashankara. High bypass ratio engine noise component separation by coherence technique. *J. Aircraft*, 20(3):236–242, 1983.

[30] T. Minami and K. K. Ahuja. Five microphone method for separating two different noise sources from farfield measurements contaminated by extraneous noise. Technical Report AIAA Paper 2003-3261, 9th AIAA/CEAS Aeroacoustic Conference, Hilton Head, South Carolina, 2003.

[31] D. K. Nance and K. K. Ahuja. Limitations of the three-microphone signal enhancement technique. Technical Report AIAA Paper 2007-0441, 45th AIAA Aerospace Sciences Meeting, Reno, Nevada, 2007.

[32] D. K. Nance. *Separating Contributions of Small-Scale Turbulence, Large-Scale Turbulence, and Core Noise from Far-Field Exhaust Noise Measurements*. PhD thesis, Georgia Institute of Technology, 2007.

[33] J. H. Miles. Spectral separation of the turbofan engine coherent combustion noise component. Technical Report AIAA Paper 2008-0050 (NASA/TM-2008-215157), 46th Aerospace Sciences Meeting, Reno, Nevada, 2008.

[34] D. R. Brillinger. *Time Series Data Analysis and Theory*. Holden-Day, 1981.

[35] J. H. Miles. Aligned and unaligned coherence: A new diagnostic tool. Technical Report AIAA Paper 2006-0010 (NASA/TM-2006-214112), 44th Aerospace Sciences Meeting, Reno, Nevada, 2006.

[36] P. D. Welch. The use of fast fourier transform for the estimation of power spectra: A method based on time averaging over short, modified periodograms. *IEEE Transactions on Audio and Electroacoustics*, AU-15(2): 70–73, 1967.

[37] H. W. Coleman and W. G. Steele. *Experimentation and Uncertainty Analysis for Engineers*. Wiley, second edition, 1999.

[38] J. S. Bendat. Statistical errors in measurement of coherence functions and input/output quantities. *J. Sound and Vibration*, 59(3):405–421, 1978.

[39] J. S. Bendat and A. G. Piersol. *Random Data Analysis and Measurement Procedures*. Wiley-Interscienceiley, second (revised and expanded) edition, 1986.